Science Advances

AAAS

advances.sciencemag.org/cgi/content/full/4/4/eaaq0148/DC1

Supplementary Materials for

Thermodynamic limit for synthesis of metastable inorganic materials

Muratahan Aykol, Shyam S. Dwaraknath, Wenhao Sun, Kristin A. Persson

Published 20 April 2018, *Sci. Adv.* **4**, eaaq0148 (2018)
DOI: 10.1126/sciadv.aaq0148

The PDF file includes:

- Supplementary Text
- figs. S1 to S42. Radial distribution functions of amorphous configurations.
- figs. S43 to S83. Bond-angle distribution functions of amorphous configurations.
- fig. S84. Amorphous limit sampling probability.
- fig. S85. Snapshots of atomic structures of amorphous materials.
- fig. S86. Probability of finding the correct, observed ground states.
- fig. S87. PDFs from aggregated uncertainties in the amorphous limit classification of crystalline polymorphs.
- table S1. The amorphous limits for the synthesizability of polymorphs.
- Legend for database S1
- References (*53–63*)

Other Supplementary Material for this manuscript includes the following:
(available at advances.sciencemag.org/cgi/content/full/4/4/eaaq0148/DC1)

- database S1 (.json format). Energies of amorphous configurations.

Supplementary Text

Descriptions of crystalline phases above the amorphous limits

There are, in total, 156 polymorphs above their respective amorphous limits in our set of material systems. Among these, 112 can be directly identified based on the available information: 45 materials have no related Inorganic Crystal Structure Database (ICSD) entry (i.e. they are hypothetical structures in the Materials Project database), 56 materials are hypothetical structures in the ICSD (e.g. Zeolites) and 11 materials are experimental high-pressure phases from the ICSD. On the other hand, there are 44 polymorphs above limits, where the structure source is in the ICSD but no further information was available to provide a description. Therefore, we investigated those separately.

Below we list the polymorphs that are above their respective amorphous limits and can be directly identified based on the available source and tagging information in the database as having no corresponding ICSD entry, as high-pressure structure, or as hypothetical structure are listed below. For each polymorph, the chemical formula is followed by the Materials Project ID (which can be used to access all relevant information at http://materialsproject.org) and tags that provide the relevant description. If there is a corresponding ICSD entry, the ICSD-number is given in square brackets. Tags provided are self-explanatory.

- Al2O3 mp-684677 No_ICSD Hypothetical_ordering_of_disordered_crystal
- Al2O3 mp-684713 No_ICSD Hypothetical_ordering_of_disordered_crystal
- Al2O3 mp-684990 No_ICSD Hypothetical_ordering_of_disordered_crystal
- Al2O3 mp-985587 No_ICSD User_submission_to_Materials_Project
- C mp-998866 No_ICSD, User_submission_to_Materials_Project
- CoO2 mvc-10954 No_ICSD High-throughput_cathode_search
- CoO2 mvc-6933 No_ICSD High-throughput_cathode_search
- Fe2O3 mvc-12005 No_ICSD High-throughput_cathode_search
- Ga2O3 mp-13134 [162252] High_pressure_ICSD. Erroneous ICSD entry: this entry was later removed from ICSD because Gd2S3 was incorrectly entered as Gd2O3.
- Ga2O3 mp-685090 No_ICSD Hypothetical_ordering_of_disordered_crystal
- GaAs mp-10048 [43951] High_pressure_ICSD. In-situ measurement performed during compression, no evidence if this structure would be preserved upon release of pressure.
- MgO mp-1009127 [248386] High-pressure_ICSD. ICSD reference reports this is a hypothetical structure.
- MgO mp-1009129 [166273] Hypothetical Part_of_two_layered_model
- MoO3 mp-705538 No_ICSD Hypothetical_ordering_of_disordered_crystal
- MoO3 mvc-11096 No_ICSD High-throughput_cathode_search
- MoO3 mvc-13534 No_ICSD High-throughput_cathode_search
- NbO2 mp-25214 No_ICSD

- P2O5 mp-689684 No_ICSD
- P2O5 mp-990076 No_ICSD User_submission_to_Materials_Project
- Si mp-1001113 No_ICSD User_submission_to_Materials_Project
- Si mp-1014212 No_ICSD User_submission_to_Materials_Project
- Si mp-10649 [52459] High_pressure_ICSD. In-situ measurement performed during compression, no evidence if such hcp-Si would be preserved upon release of pressure.
- Si mp-27 [52458, 57187] High_pressure_ICSD. In-situ measurement performed during compression, no evidence if such fcc-Si would be preserved upon release of pressure.
- Si mp-644693 [109036] High_pressure_ICSD. ICSD Reference confirms this phase is yielded by a reversible transformation; i.e. is not preserved upon release of pressure.
- Si mp-676011 [109036] High_pressure_ICSD. See the entry above.
- Si3N4 mp-40793 No_ICSD Hypothetical_ordering_of_disordered_crystal
- SiO2 mp-12350 [170476] Hypothetical_Zeolite_ICSD
- SiO2 mp-32667 No_ICSD Hypothetical_ordering_of_disordered_crystal
- SiO2 mp-34150 No_ICSD Hypothetical_ordering_of_disordered_crystal
- SiO2 mp-545488 [170548] Hypothetical_Zeolite_ICSD
- SiO2 mp-545719 [170510] Hypothetical_Zeolite_ICSD
- SiO2 mp-554397 [170551] Hypothetical_Zeolite_ICSD
- SiO2 mp-554498 [170519] Hypothetical_Zeolite_ICSD
- SiO2 mp-554665 [170500] Hypothetical_Zeolite_ICSD
- SiO2 mp-555355 [170522] Hypothetical_Zeolite_ICSD
- SiO2 mp-555394 [171735] Hypothetical_Cluster_ICSD
- SiO2 mp-555411 [170531] Hypothetical_Zeolite_ICSD
- SiO2 mp-555497 [170508] Hypothetical_Zeolite_ICSD
- SiO2 mp-555544 [170501] Hypothetical_Zeolite_ICSD
- SiO2 mp-555676 [170533] Hypothetical_Zeolite_ICSD
- SiO2 mp-555823 [170520] Hypothetical_Zeolite_ICSD
- SiO2 mp-556027 [170539] Hypothetical_Zeolite_ICSD
- SiO2 mp-556044 [170495] Hypothetical_Zeolite_ICSD
- SiO2 mp-556068 [170475] Hypothetical_Zeolite_ICSD
- SiO2 mp-556132 [170549] Hypothetical_Zeolite_ICSD
- SiO2 mp-556257 [170478] Hypothetical_Zeolite_ICSD
- SiO2 mp-556464 [170554] Hypothetical_Zeolite_ICSD
- SiO2 mp-556537 [170507] Hypothetical_Zeolite_ICSD
- SiO2 mp-556564 [170503] Hypothetical_Zeolite_ICSD
- SiO2 mp-556812 [170544] Hypothetical_Zeolite_ICSD
- SiO2 mp-556963 [170521] Hypothetical_Zeolite_ICSD

- SiO2 mp-557017 [170537] Hypothetical_Zeolite_ICSD
- SiO2 mp-557076 [170514] Hypothetical_Zeolite_ICSD
- SiO2 mp-557194 [170552] Hypothetical_Zeolite_ICSD
- SiO2 mp-557723 [170523] Hypothetical_Zeolite_ICSD
- SiO2 mp-557771 [170492] Hypothetical_Zeolite_ICSD
- SiO2 mp-557814 [170488] Hypothetical_Zeolite_ICSD
- SiO2 mp-558366 [170535] Hypothetical_Zeolite_ICSD
- SiO2 mp-558598 [170506] Hypothetical_Zeolite_ICSD
- SiO2 mp-558733 [41673] High_pressure_ICSD. ICSD Reference confirms this is a hypothetical structure.
- SiO2 mp-558931 [170505] Hypothetical_Zeolite_ICSD
- SiO2 mp-559389 [170553] Hypothetical_Zeolite_ICSD
- SiO2 mp-559605 [170540] Hypothetical_Zeolite_ICSD
- SiO2 mp-559829 [170477] Hypothetical_Zeolite_ICSD
- SiO2 mp-559860 [170527] Hypothetical_Zeolite_ICSD
- SiO2 mp-560754 [170502] Hypothetical_Zeolite_ICSD
- SiO2 mp-560836 [170489] Hypothetical_Zeolite_ICSD
- SiO2 mp-560954 [170529] Hypothetical_Zeolite_ICSD
- SiO2 mp-561291 [170532] Hypothetical_Zeolite_ICSD
- SiO2 mp-561301 [170483] Hypothetical_Zeolite_ICSD
- SiO2 mp-561488 [170486] Hypothetical_Zeolite_ICSD
- SiO2 mp-572283 [170530] Hypothetical_Zeolite_ICSD
- SiO2 mp-600096 No_ICSD
- SiO2 mp-638033 [170550] Hypothetical_Zeolite_ICSD
- SiO2 mp-638035 [170515] Hypothetical_Zeolite_ICSD
- SiO2 mp-638038 [170538] Hypothetical_Zeolite_ICSD
- SiO2 mp-638049 [170504] Hypothetical_Zeolite_ICSD
- SiO2 mp-673168 No_ICSD Hypothetical_ordering_of_disordered_crystal
- SiO2 mp-683947 [170536] Hypothetical_Zeolite_ICSD
- SiO2 mp-683952 [170487] Hypothetical_Zeolite_ICSD
- SiO2 mp-683953 [170484] Hypothetical_Zeolite_ICSD
- SiO2 mp-685184 No_ICSD Hypothetical_ordering_of_disordered_crystal
- SiO2 mp-6947 [9160, 10078, 20604, 36226, 40098, 40099, 40100, 40101, 40102, 40103, 40104, 40105, 40106, 41668, 41671, 44096, 51701, 68158, 68159, 68160, 68161, 68162, 68163, 68164, 68165, 68166, 68409, 68410, 73073, 74531, 75740, 77523, 92550, 93548, 93549, 93550, 93551, 97181, 97182, 98632, 98633, 109195, 158527, 158528, 158529, 158530, 158531, 158532, 158533, 158534, 158535, 158536, 162631, 162632] High_pressure_ICSD. This is the stishovite polymorph that is known to become at low pressures as discussed in the manuscript.

- SiO2 mp-7905 No_ICSD
- SiO2 mp-9258 [70016, 158958, 181307, 181308, 181309, 181310] High_pressure_ICSD. In-situ measurement performed during compression, no evidence if this phase would be preserved upon release of pressure.
- SnO mp-999142 [185350] Hypothetical
- SnO2 mp-562610 [157454, 181282, 181283] High_pressure_ICSD
- SnO2 mvc-13245 No_ICSD High-throughput_cathode_search
- SnO2 mvc-6071 No_ICSD High-throughput_cathode_search
- SnO2 mvc-9896 No_ICSD High-throughput_cathode_search
- Ta2O5 mp-676422 No_ICSD Hypothetical_ordering_of_disordered_crystal
- Ta2O5 mvc-8453 No_ICSD High-throughput_cathode_search
- TaN mp-1009831 [183426] Hypothetical
- TaN mp-1009833 [67876] Hypothetical
- TaN mp-570454 [76457] High_pressure_ICSD. The other entry for the hexagonal ϵ-TaN (P6/mmm) is below the amorphous limit. Inspection of this structure indicates Ta and N sites were erroneously assigned to the opposite specie in the entry.
- TiO2 mp-1008677 [189325] Hypothetical
- TiO2 mp-25262 No_ICSD
- TiO2 mp-572822 No_ICSD
- TiO2 mvc-11115 No_ICSD High-throughput_cathode_search
- TiO2 mvc-11912 No_ICSD High-throughput_cathode_search
- TiO2 mvc-13391 No_ICSD High-throughput_cathode_search
- TiO2 mvc-4715 No_ICSD High-throughput_cathode_search
- TiO2 mvc-5171 No_ICSD High-throughput_cathode_search
- TiO2 mvc-9726 No_ICSD High-throughput_cathode_search
- VO2 mp-714931 No_ICSD
- VO2 mvc-11089 No_ICSD High-throughput_cathode_search
- VO2 mvc-11154 No_ICSD High-throughput_cathode_search
- WO2 mvc-10022 No_ICSD High-throughput_cathode_search
- WO2 mvc-11221 No_ICSD High-throughput_cathode_search
- WO3 mvc-11457 No_ICSD High-throughput_cathode_search
- WO3 mvc-13988 No_ICSD High-throughput_cathode_search
- Y2O3 mp-673247 No_ICSD Hypothetical_ordering_of_disordered_crystal

Below we list the polymorphs that are above their respective amorphous limits and have a corresponding ICSD entry, but have no further information in database to describe why structure is above the amorphous limit. Therefore, these structures are inspected manually. Chemical formula of the polymorph is followed by the Materials Project ID (which can be used to access all relevant information at http://materialsproject.org) and a short description. The ICSD-numbers are given in square brackets.

- Al2O3 mp-638765 [173014] Description: Unphysical ICSD structure. Possibly erroneous CIF file.
- Al2O3 mp-642363 [161062] Description: Hypothetical structure in the ICSD.
- AlF3 mp-635425 [30274] Description: Erroneous CIF file.
- BeO mp-1794 [26957, 162676, 163825, 163826, 163827, 163828, 163829] Description: Hypothetical, or possibly very high pressure. This NaCl type polymorph of BeO extensively tested with theory since all other alkaline earth oxides are NaCl type.
- BN mp-601223 [27986] Description: Erroneous structure for the well-known form hexagonal BN.
- C mp-579909 [88812] Description: Hypothetical structure in the ICSD.
- C mp-624889 [88811, 88815] Description: Hypothetical structure in the ICSD.
- CoO2 mp-556750 [54958, 95440] Description: Part of a modulated superstructure.
- CoO mp-19275 [53059] Description: Problematic calculation. This is the NaCl (Fm3m) structure (mp-19079) with tetragonal distortion (I4/mmm). Lack of magnetic ordering might have led to metastable DFT+U state in this case, as the Fm3m analog is already much lower in energy. This should have relaxed close to the energy of the Fm3m phase (mp-19079) if there were no calculation issues.
- Fe2O3 mp-609465 [36281] Description: Problematic magnetic ordering. Ferromagnetically ordered DFT+U calculation of the same structure (beta Fe2O3) is more stable and below the amorphous limit.
- Fe2O3 mp-716814 [36281] Description: See the previous entry.
- FeO mp-18905 [27856, 31081, 53519, 60683, 76639, 82233, 82236, 180972, 180973, 180974, 633029, 633031, 633036, 633038] Description: Problematic magnetic ordering. Anti-ferromagnetic ordering is more stable and below the amorphous limit.
- NbO2 mp-649729 [8244] Description: Same structure from neutron diffraction (e.g. ICSD number 96) relaxed properly and is the ground state in the Materials Project (mp-821). This particular structure has a complication either in the structure source or in the computation.
- SiO2 mp-10948 [161310] Description: Erroneous CIF file.
- SiO2 mp-553881 [75668] Description: Hypothetical structure in the ICSD.
- SiO2 mp-556588 [75667] Description: Hypothetical structure in the ICSD.
- SiO2 mp-558301 [171736] Description: Hypothetical structure in the ICSD.
- SiO2 mp-640917 [155252] Description: Amorphous-like structure reported.
- SiO2 mp-10064 [44271] Description: Hypothetical structure in the ICSD.
- SiO2 mp-556788 [75666] Description: Hypothetical structure in the ICSD.
- SiO2 mp-557653 [75665] Description: Hypothetical structure in the ICSD.
- SiO2 mp-559741 [51702, 161310] Description: Rare high-pressure phase, often found on Mars.
- SiO2 mp-559273 [171734] Description: Hypothetical structure in the ICSD.
- SiO2 mp-683970 [171742] Description: Hypothetical structure in the ICSD.
- SiO2 mp-556319 [75660] Description: Hypothetical structure in the ICSD.
- SiO2 mp-556880 [75663] Description: Hypothetical structure in the ICSD.
- SiO2 mp-555960 [171733] Description: Hypothetical structure in the ICSD.

- SiO2 mp-604717 [162625] Description: This particular structure listed as Keatite is from a computational study. Keatite as obtained from another ICSD entry (mp-559872) is already found to be very close to convex-hull, and below the amorphous limit.
- SiO2 mp-557244 [75664] Description: Hypothetical structure in the ICSD.
- SiO2 mp-667448 [83332] Description: Structure derived using a lattice energy minimization based search, attempted to explain NMR data.
- SiO2 mp-556376 [75669] Description: Hypothetical structure in the ICSD.
- Si mp-16220 [56721] Description: Hypothetical structure in the ICSD.
- Si3N4 mp-583712 [67241] Description: Hypothetical structure in the ICSD.
- Si3N4 mp-568867 [16752] Description: alpha-Si3N4, as calculated from other ICSD sources [90146 164618 35560 35561 35562 35563 35564 35565 26191 34096 77811 79797 92156 644682], is already found to be the groundstate in Materials Project database. This particular structure is erroneous.
- Si3N4 mp-603694 [159207] Description: See the previous entry for the ICSD numbers for alpha groundstate in Materials Project. This particular report of the alpha structure is originating from a theoretical study.
- Ta2O5 mp-554867 [95462] Description: Structures of low temperature Ta2O5 (including beta and Z) are problematic. According to Wu et al. (*53*), both are dynamically unstable and their symmetry needs to be lowered compared to experimental reports, which lowers their energy in GGA by about 0.25 eV/atom via distortions. Therefore, this high-symmetry entry does not provide the correct GGA energy.
- Ta2O5 mp-624688 [280397] Description: See description provided for the previous entry.
- TiO2 mp-636827 [97008] Description: Surface reconstruction of SrTiO3, not the representative bulk structure.
- TiO2 mp-655656 [97008] Description: See the previous entry.
- V2O5 mp-624689 [43132] Description: Problem with the crystal structure. Reports of the same mineral (e.g. ICSD 99808 157988 647638 653926 82151 82152 24042 40488 15798 94904 41030 60767) are identical and found to be the groundstate.
- VO2 mp-636976 [1501] Description: Structure looks unusual. There has to be V-O octahedra as also referred in the original paper by Ghedira et al. (*54*), which are not reproduced in the structure obtained from the corresponding CIF file. Erroneous entry.
- VO2 mp-636921 [1503] Description: See the previous entry.
- VO2 mp-566801 [1503] Description: See the previous entry.
- ZnO mp-13161 [163382, 182360] Description: Hypothetical (possibly very high pressure) structure.

<u>Accuracy of density functional theory in predicting the amorphous limit and relative stabilities of polymorphs</u>

Recent studies show that the average density functional theory (DFT) with Perdew-Burke-Ernezerhof functional (PBE) errors in “formation energies” vary from ~0.05 to ~0.1 eV/atom (*14*, *55*, *56*), which are further found to be comparable to the level of

disparities among experimental formation energies (*14*). Therefore, the "error" in formation energies in fact cannot be solely attributed to PBE either. More importantly, typical errors associated with comparing energies of compounds of similar chemistries within the same chemical system (rather than formation energies with respect to elemental reference states) are known to be much smaller. Hautier et al. (*38*) did a thorough analysis of reaction energies between binary and ternary compounds in the same chemical systems and showed the mean absolute error in PBE reaction energies among such compounds with respect to a well-curated set of experimental energies is close to zero (i.e. indicating no obvious systematic error), with a standard deviation of ~24 meV/atom due to substantial error cancellation when similar chemistries are compared. Therefore, considering that we are comparing "polymorphs" that have the same chemical constituents and composition, ~24 meV/atom is likely an upper-bound for the typical errors we would expect from PBE in the present study. To estimate the range of possible DFT errors specifically in measuring the relative energies of polymorphs, we performed a series of statistical simulations presented in fig. S86. We observe that the maximum permissible level of random DFT errors drawn from a Gaussian distribution with standard deviation of σ to correctly produce the groundstate (as it is already achieved by DFT in these systems) within 5 meV/atom, with a probability of at least 90%, are σ of ~12, ~8, ~5 and ~2 meV/atom for Al_2O_3, GaN, V_2O_5 and ZnS, respectively, with slightly smaller values for exactly identifying the groundstate and slightly larger values for a tolerance of 10 meV/atom. While a more thorough analysis of DFT errors in polymorphic systems is required for more accurate assessments, these observations at least imply that possible random DFT errors in measuring relative energies of polymorphs show some chemistry dependence, and are likely much smaller compared to 24 meV/atom estimated for compound reaction energies by Hautier et al. (*38*), as we expected, and likely around ~12 meV/atom or below. Such DFT errors in polymorphic systems are expected to be rather non-random, arising from structure and chemistry specific deficiencies of DFT calculations, including but not limited to the lack of van der Waals interactions, inadequate magnetic configurations or pseudopotentials, lack of proper description of correlation effects, and other inadequacies of the exchange-correlation functional used.

Statistical evaluation of the aggregated uncertainties in amorphous energies and DFT

We performed further statistical simulations presented in fig. S87 to measure the probability that *at least one material that has been synthesized is misclassified as unsynthesizable* due to aggregated uncertainties of amorphous energies and random DFT errors, both described separately in Materials and Methods and Supplementary Text. We evaluate such probability distributions as a function of sample size *n* of amorphous energies and with multiple zero-centered Gaussian-distributions for random DFT errors described by standard-deviations (σ) ranging from the largest σ of ~12 meV/atom estimated above to the ~24 meV/atom upper-bound estimate by Hautier et al. (*38*). We observe in fig. S87 that there is a certain amount of cancellation between the random DFT error and the unidirectional (only positive) sampling error in amorphous energies (See Fig. 4) in the final aggregated PDFs. We set the *amorphous energy = synthesis limit* as our *null* hypothesis. Finally, we show in fig. S87 that the alternative hypothesis *amorphous energy < synthesis limit* can be rejected on the basis of existing amorphous

data and reasonable ranges of random DFT errors as estimated above for polymorphic systems.

Atomic structures of amorphous configurations.

As shown in fig. S1, for amorphous Al_2O_3, the partial radial distribution functions obtained from the final, optimized amorphous structures are in good agreement with the experimental results of Lamparter and Kniep (*45*) (where partial functions were obtained by reverse Monte Carlo simulation of X-ray and neutron diffraction data). The experimental Al-O, O-O and Al-Al bond distances of 1.8, 2.8, and 3.2 Å, respectively, also agree well with the peak positions in fig. S1.

Figures S2-S42 show the partial radial distribution functions (RDFs), $g_{ij}(r)$, of amorphous structures and their ab-initio molecular dynamics (AIMD) generated liquids in 41 material systems considered in this work, where solid and open-circles connected with dashed lines correspond to liquid and amorphous phases, respectively. The densities (ρ) of the liquid and amorphous structures are also shown as insets. Bond-angle distribution functions (BDFs) of the amorphous structures are shown in figs. S43-S83. The BDFs are denoted in the form X-Y-Z, where the angle between X-Y and Y-Z vectors are measured; i.e., Y is the central atom in the triplet. A five-point Savitzky-Golay filter was applied to both RDFs and BDFs to obtain smoother functions for better visualization.

All liquids are observed to have a well-defined short range order, but still have very broad RDF peaks, with little to no order beyond first coordination shells. In amorphous structures, the intensity of the RDF peaks increase significantly relative to liquids, signaling the increase in short-range order. Generally, hetero-chemical coordination is highly favored, and no substantial nearest-neighbor coordination is observed between identical species. Exceptions to this observation are small amounts of N-N or O-O coordinations, for instance, in BN, GaN, Si_3N_4, and a few oxides such as CoO_2, In_2O_3 and P_2O_5. Homopolar coordinations were also observed in previous molecular simulations of similar amorphous materials in literature (*57–60*). Overall, RDFs show successful *ab-initio* generation of amorphous structures, with well-captured short-range order.

For most of the amorphous structures, BDFs are broad, concentrating around certain angles pertaining to local packing of hetero-coordinated species (e.g. in 3-, 4-, 5- and 6-fold coordinated structural units), as expected from the disordered packing of a distribution of such local units in amorphous materials. Systems with exceptionally sharp BDFs that deviate from this general trend are that of network forming oxides B_2O_3 and Si_2O_3, and BN, shown in fig. S45, S69, and S46, respectively. Amorphous B_2O_3 is comprised of B-centered triangular BO_3 units analogous to its crystalline counterpart, some of which also form boroxol rings, which gives rise to sharp peaks in O-B-O, B-O-O and O-O-O BDFs. The broad B-B-B BDF in the amorphous B_2O_3 shows the packing of these units is in fact highly disordered. These findings are consistent with the previous reports in literature (*61*). Amorphous SiO_2 also has a rigid local unit, the well-known tetrahedral SiO_4 packing, giving rise to sharp peaks in BDFs, which are also packed disorderly as evident from the broad Si-Si-Si BDF, again in agreement with the current

understanding of vitreous silica (*62*, *63*). Sharp peaks in all BDFs of BN arise from the formation of small but well-defined regions of nearly planar hexagonal B-N rings in the amorphous phase, analogous to the hexagonal graphite-type symmetry in the crystalline BN and occasional. Similar observations were also reported in a recent ab-initio molecular dynamics study of amorphous BN (*57*).

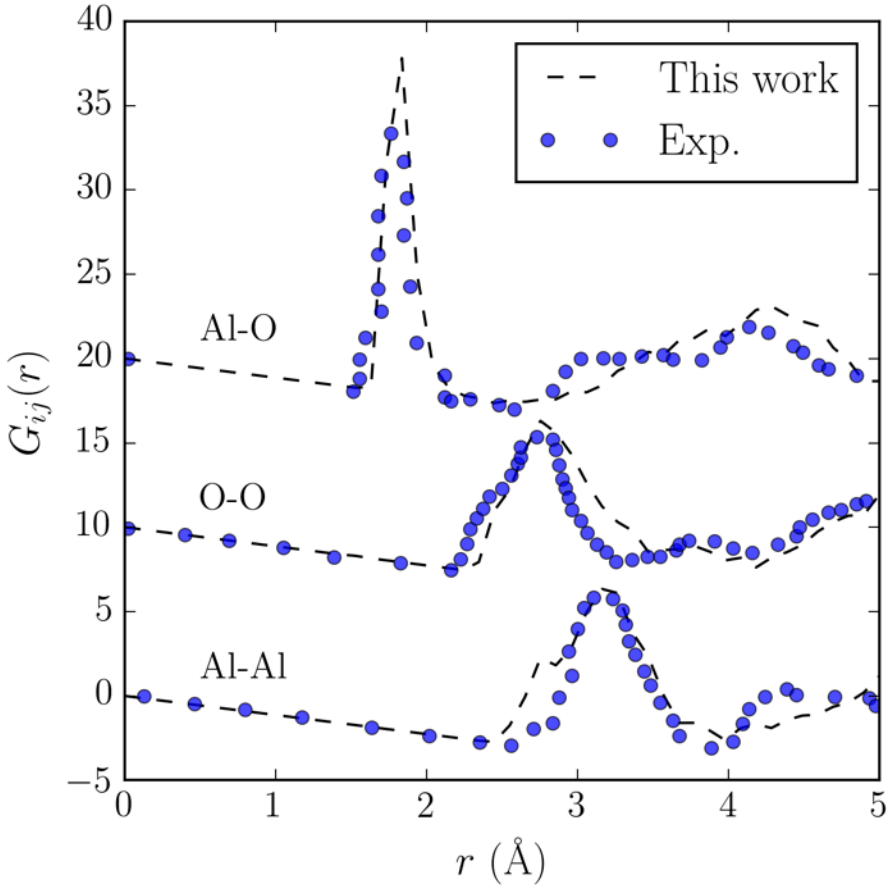

fig. S1. Radial distribution functions of amorphous configurations. Comparison of the partial radial distribution functions of AIMD + DFT relaxation computed amorphous Al_2O_3 snapshots with experimental data from Lamparter and Kneip (*49*). $\boldsymbol{g_{ij}(r)}$ is converted to the $\boldsymbol{G_{ij}(r) = 4r[g_{ij}(r) - 1]}$ for comparison.

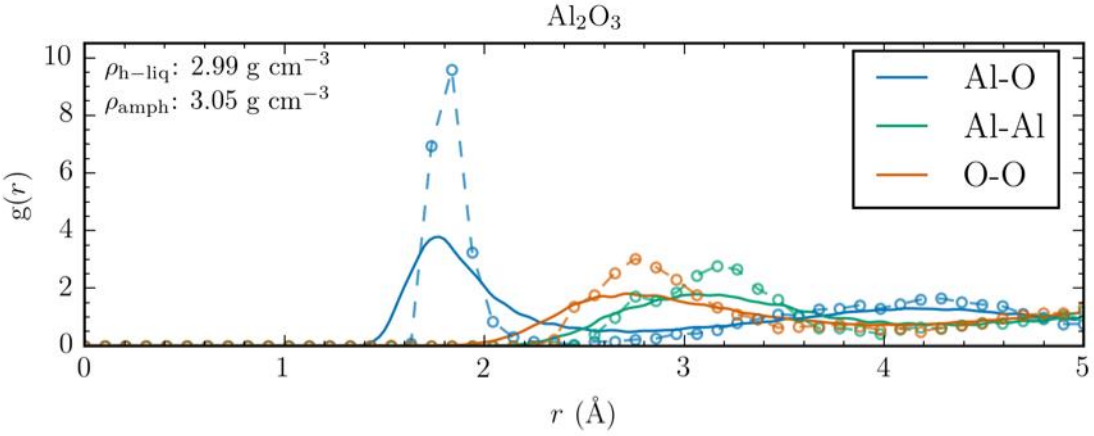

fig. S2. Radial distribution functions of amorphous configurations. Partial radial distribution functions of AIMD-generated amorphous Al_2O_3 and the parent high-temperature hypothetical liquid that amorphous configurations are quenched from.

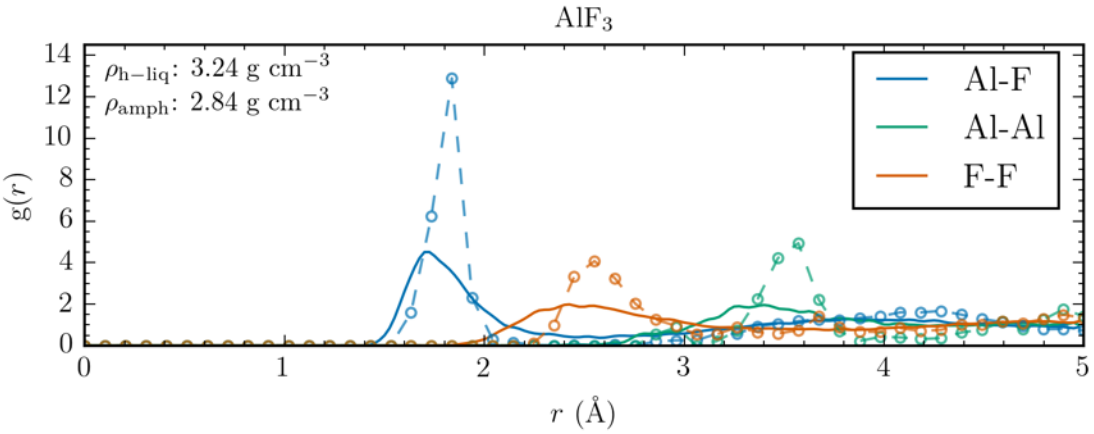

fig. S3. Radial distribution functions of amorphous configurations. Partial radial distribution functions of AIMD-generated amorphous AlF_3 and the parent high-temperature hypothetical liquid that amorphous configurations are quenched from.

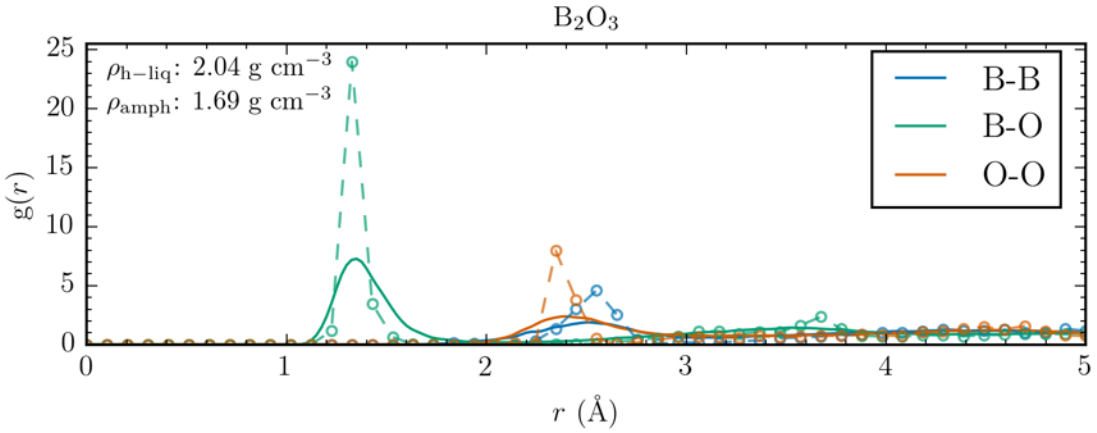

fig. S4. Radial distribution functions of amorphous configurations. Partial radial distribution functions of AIMD-generated amorphous B_2O_3 and the parent high-temperature hypothetical liquid that amorphous configurations are quenched from.

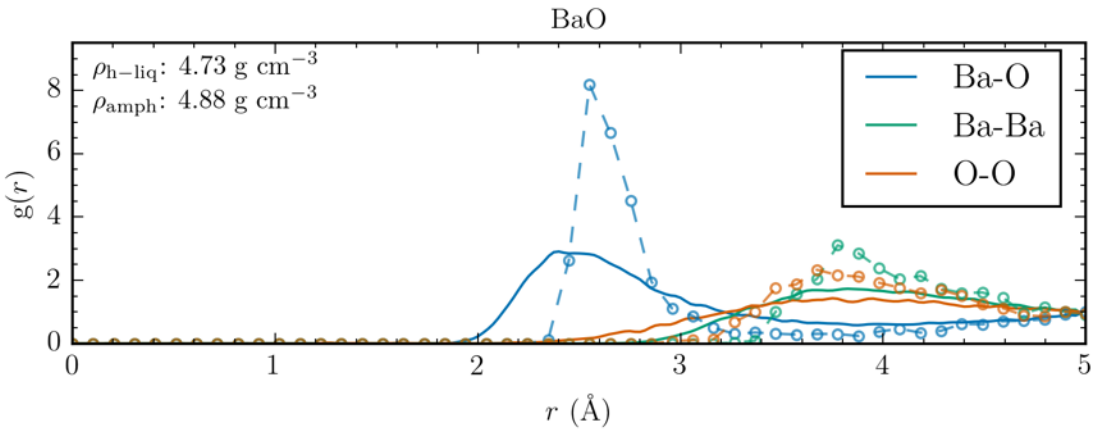

fig. S5. Radial distribution functions of amorphous configurations. Partial radial distribution functions of AIMD-generated amorphous BaO and the parent high-temperature hypothetical liquid that amorphous configurations are quenched from.

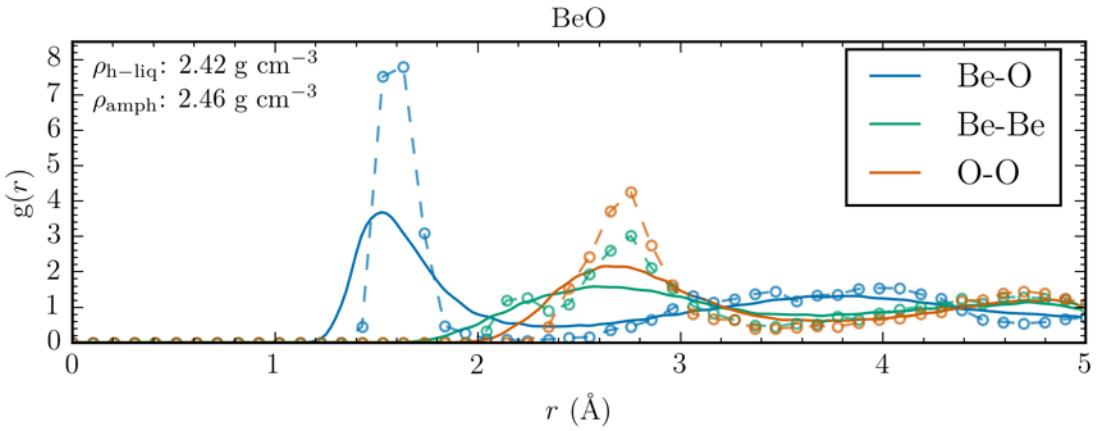

fig. S6. Radial distribution functions of amorphous configurations. Partial radial distribution functions of AIMD-generated amorphous BeO and the parent high-temperature hypothetical liquid that amorphous configurations are quenched from.

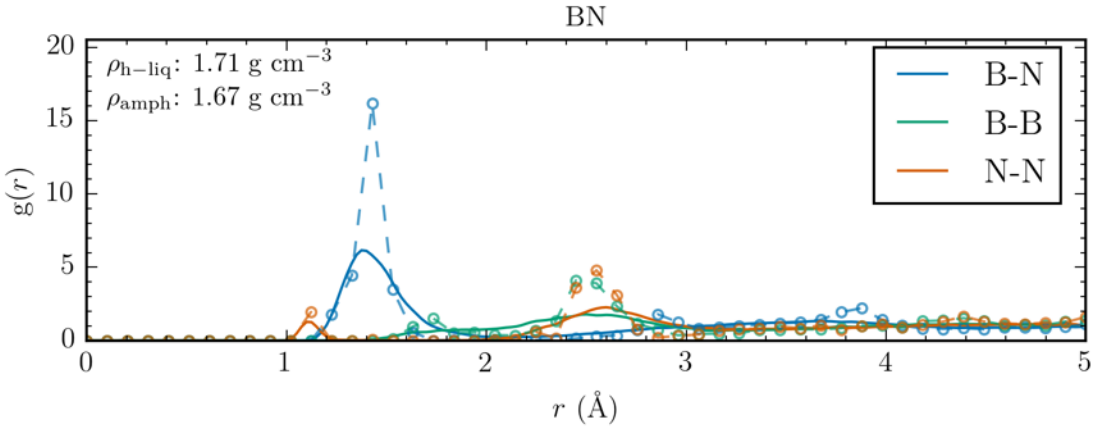

fig. S7. Radial distribution functions of amorphous configurations. Partial radial distribution functions of AIMD-generated amorphous BN and the parent high-temperature hypothetical liquid that amorphous configurations are quenched from.

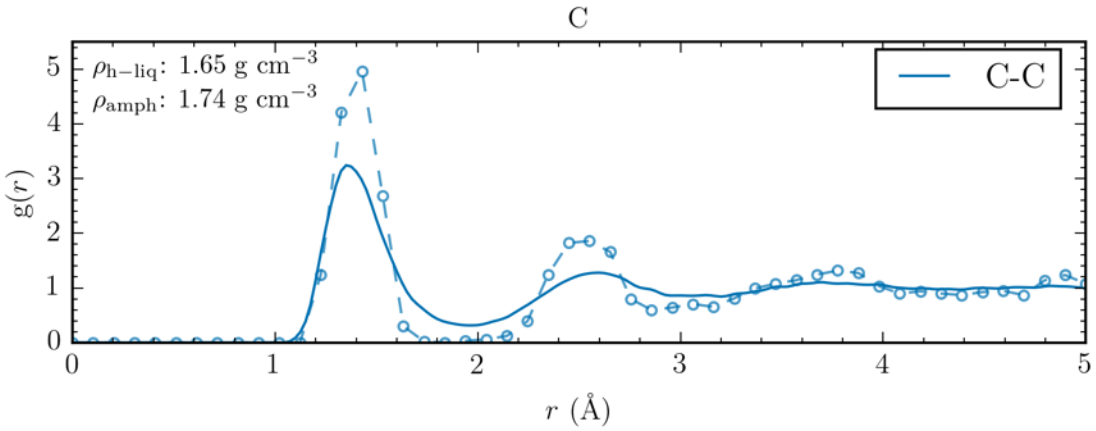

fig. S8. Radial distribution functions of amorphous configurations. Partial radial distribution functions of AIMD-generated amorphous C and the parent high-temperature hypothetical liquid that amorphous configurations are quenched from.

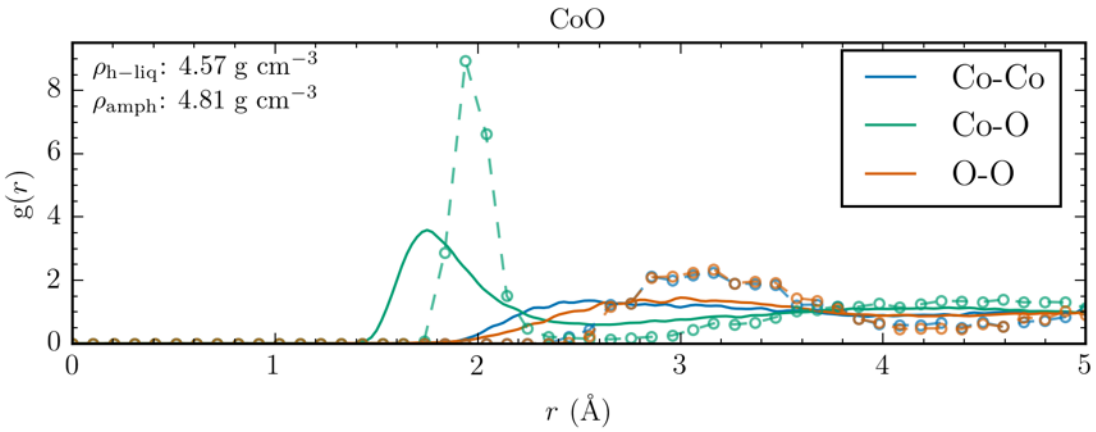

fig. S9. Radial distribution functions of amorphous configurations. Partial radial distribution functions of AIMD-generated amorphous CoO and the parent high-temperature hypothetical liquid that amorphous configurations are quenched from.

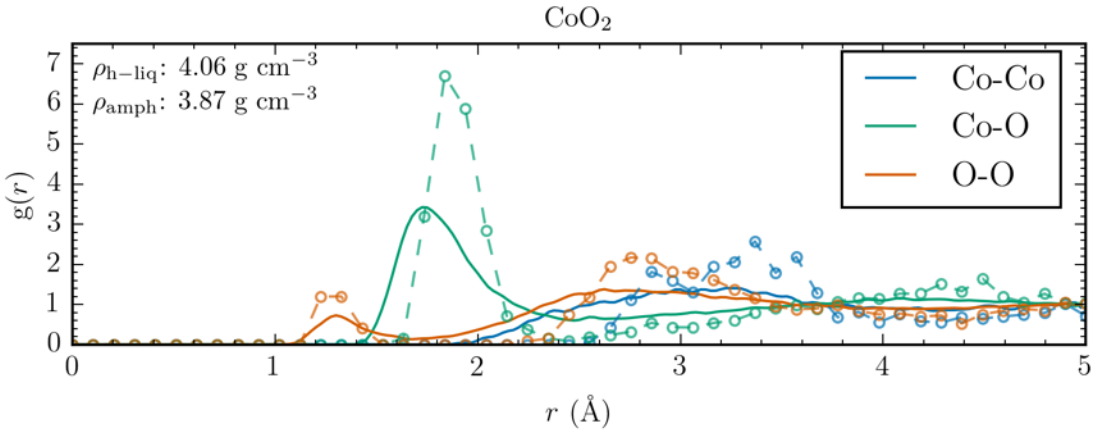

fig. S10. Radial distribution functions of amorphous configurations. Partial radial distribution functions of AIMD-generated amorphous CoO_2 and the parent high-temperature hypothetical liquid that amorphous configurations are quenched from.

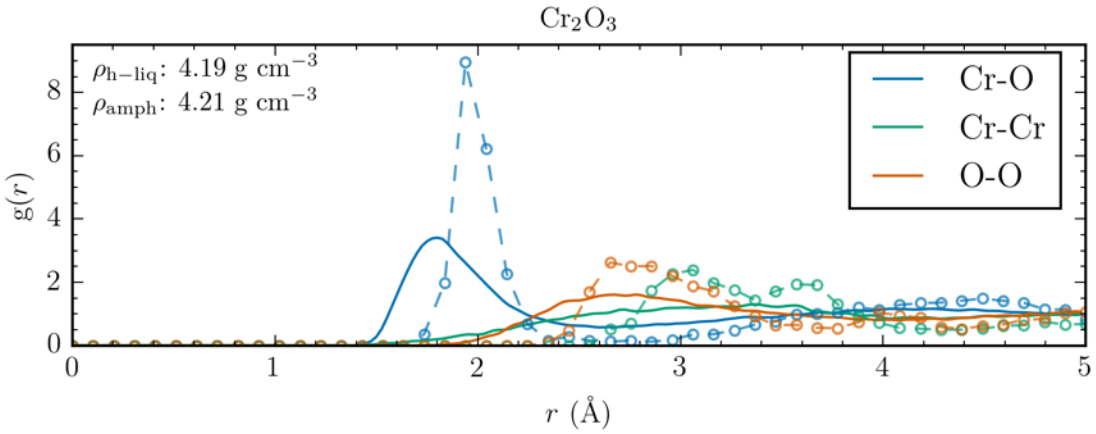

fig. S11. Radial distribution functions of amorphous configurations. Partial radial distribution functions of AIMD-generated amorphous Cr_2O_3 and the parent high-temperature hypothetical liquid that amorphous configurations are quenched from

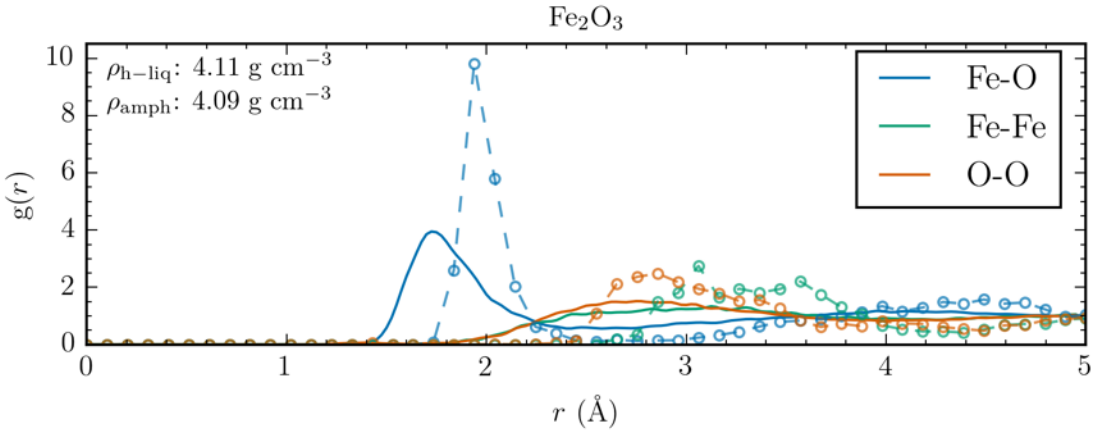

fig. S12. Radial distribution functions of amorphous configurations. Partial radial distribution functions of AIMD-generated amorphous Fe_2O_3 and the parent high-temperature hypothetical liquid that amorphous configurations are quenched from.

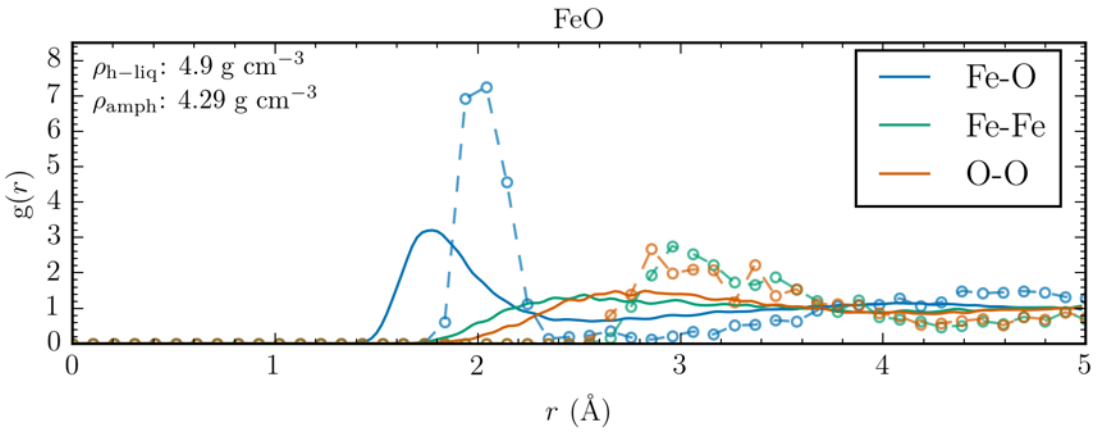

fig. S13. Radial distribution functions of amorphous configurations. Partial radial distribution functions of AIMD-generated amorphous FeO and the parent high-temperature hypothetical liquid that amorphous configurations are quenched from.

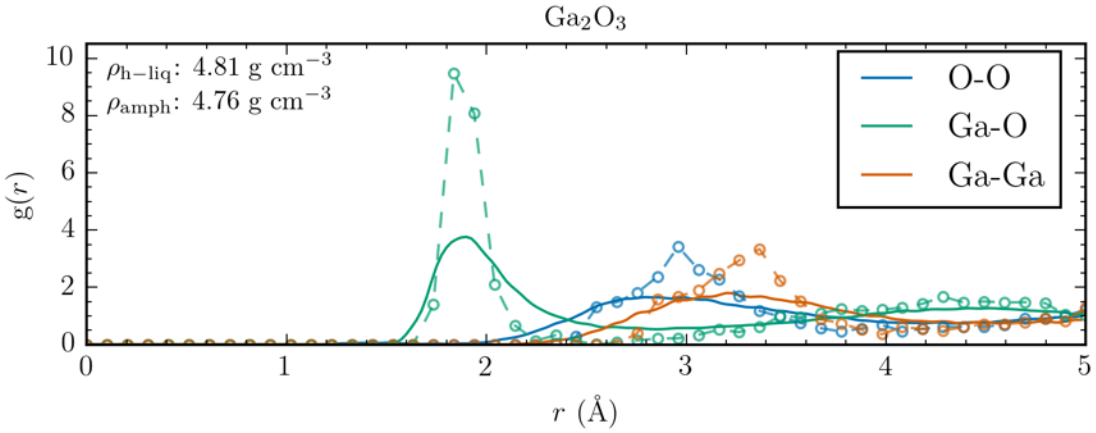

fig. S14. Radial distribution functions of amorphous configurations. Partial radial distribution functions of AIMD-generated amorphous Ga_2O_3 and the parent high-temperature hypothetical liquid that amorphous configurations are quenched from.

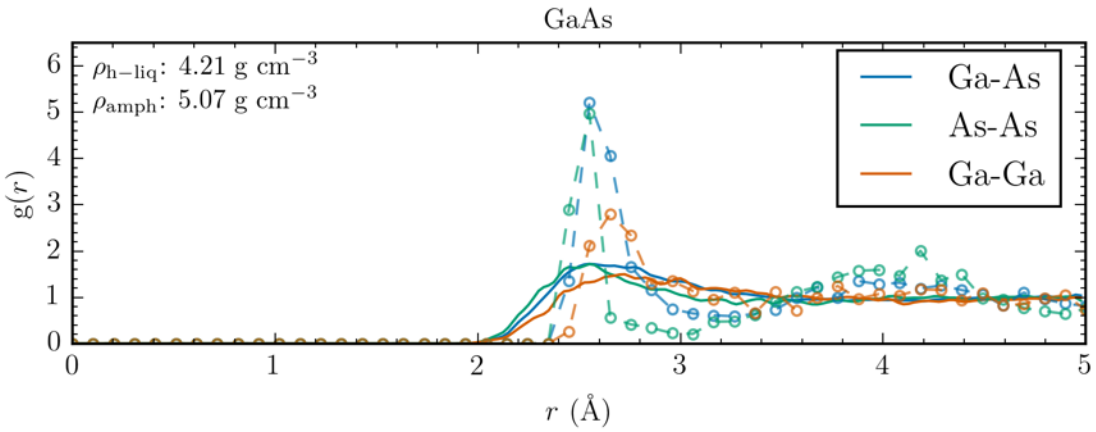

fig. S15. Radial distribution functions of amorphous configurations. Partial radial distribution functions of AIMD-generated amorphous GaAs and the parent high-temperature hypothetical liquid that amorphous configurations are quenched from.

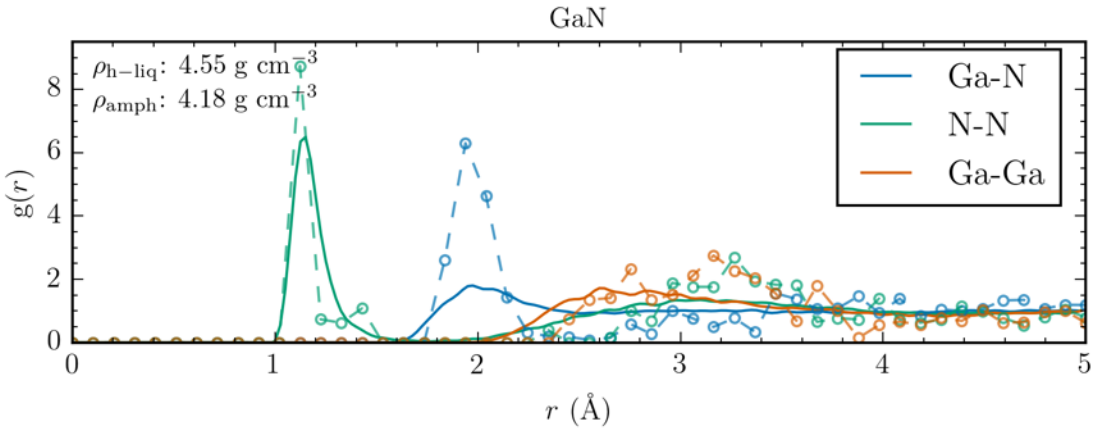

fig. S16. Radial distribution functions of amorphous configurations. Partial radial distribution functions of AIMD-generated amorphous GaN and the parent high-temperature hypothetical liquid that amorphous configurations are quenched from.

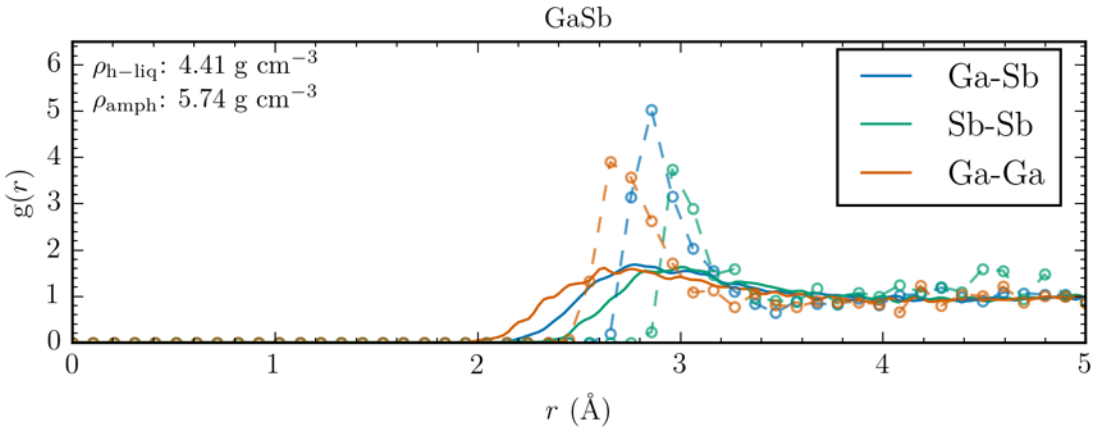

fig. S17. Radial distribution functions of amorphous configurations. Partial radial distribution functions of AIMD-generated amorphous GaSb and the parent high-temperature hypothetical liquid that amorphous configurations are quenched from.

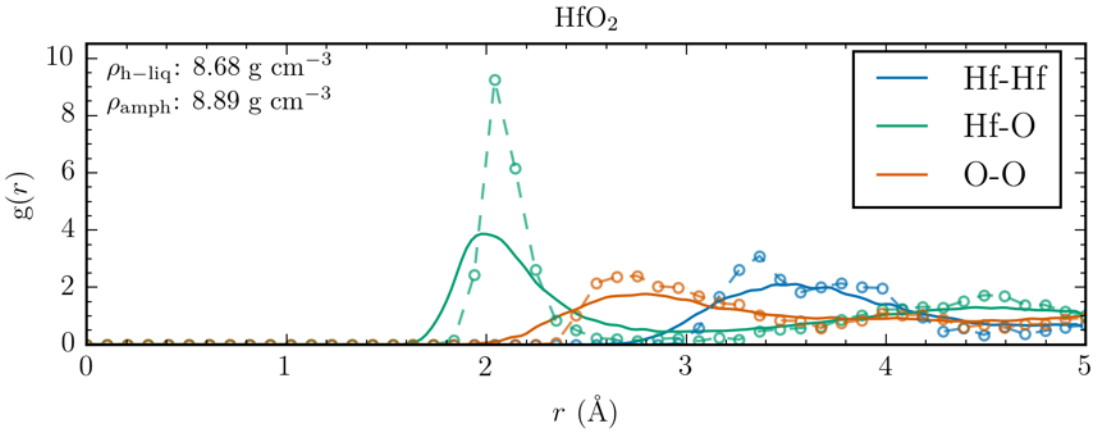

fig. S18. Radial distribution functions of amorphous configurations. Partial radial distribution functions of AIMD-generated amorphous HfO_2 and the parent high-temperature hypothetical liquid that amorphous configurations are quenched from.

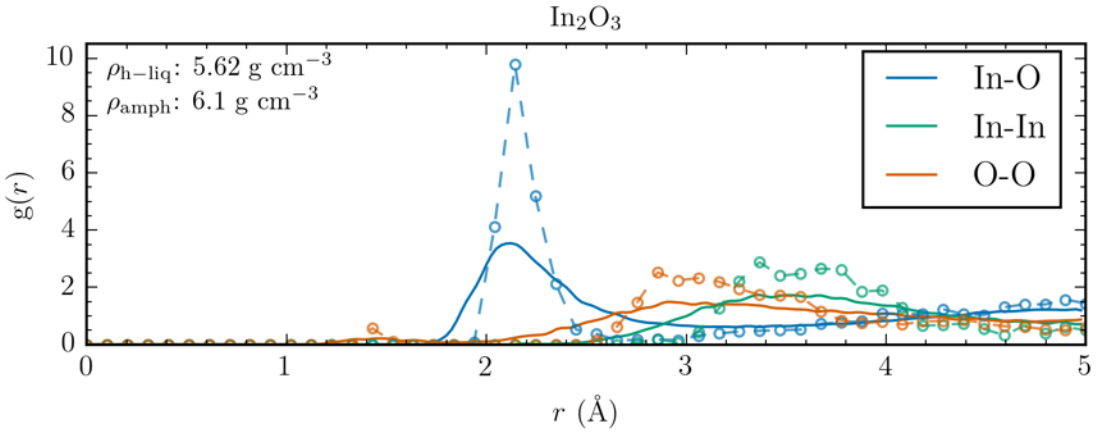

fig. S19. Radial distribution functions of amorphous configurations. Partial radial distribution functions of AIMD-generated amorphous In_2O_3 and the parent high-temperature hypothetical liquid that amorphous configurations are quenched from.

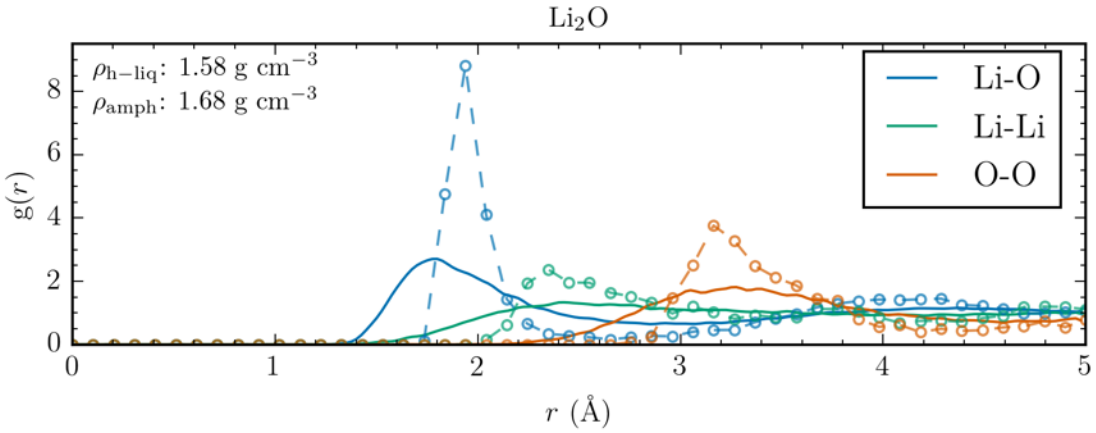

fig. S20. Radial distribution functions of amorphous configurations. Partial radial distribution functions of AIMD-generated amorphous Li_2O and the parent high-temperature hypothetical liquid that amorphous configurations are quenched from.

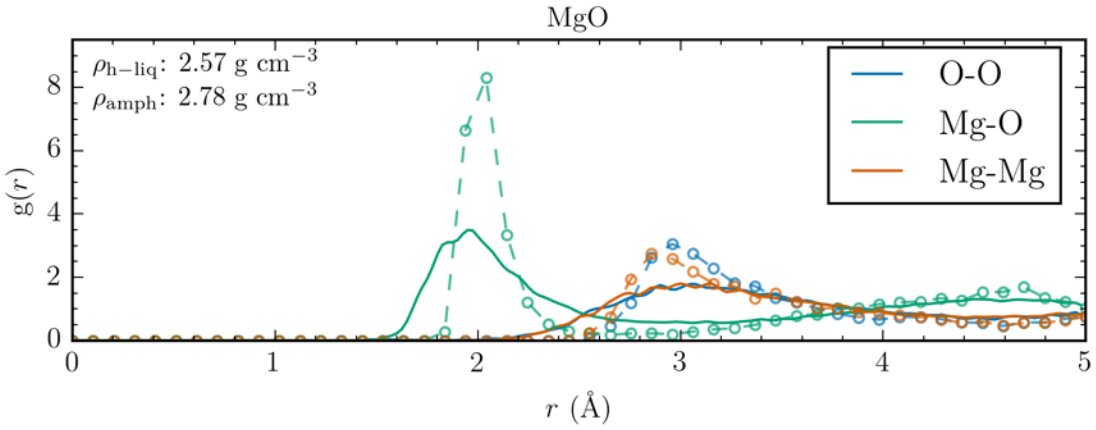

fig. S21. Radial distribution functions of amorphous configurations. Partial radial distribution functions of AIMD-generated amorphous MgO and the parent high-temperature hypothetical liquid that amorphous configurations are quenched from.

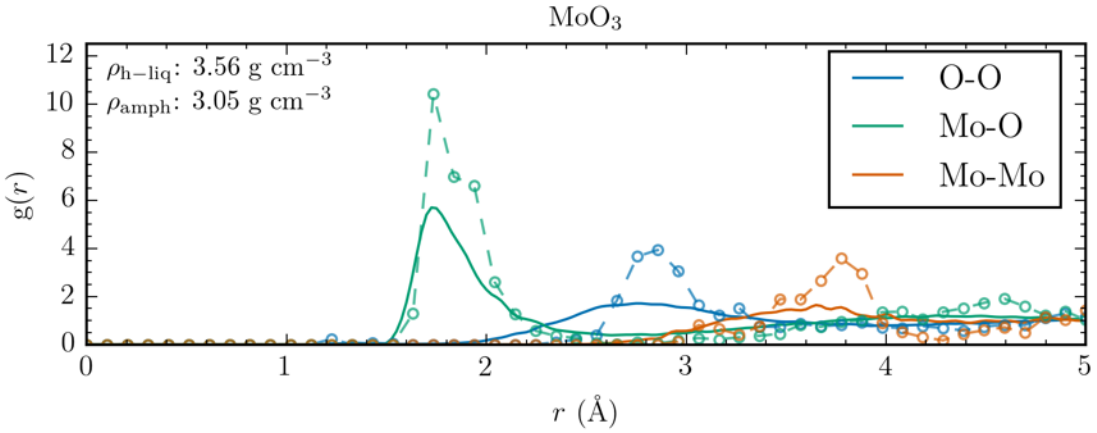

fig. S22. Radial distribution functions of amorphous configurations. Partial radial distribution functions of AIMD-generated amorphous B_2O_3 and the parent high-temperature hypothetical liquid that amorphous configurations are quenched from.

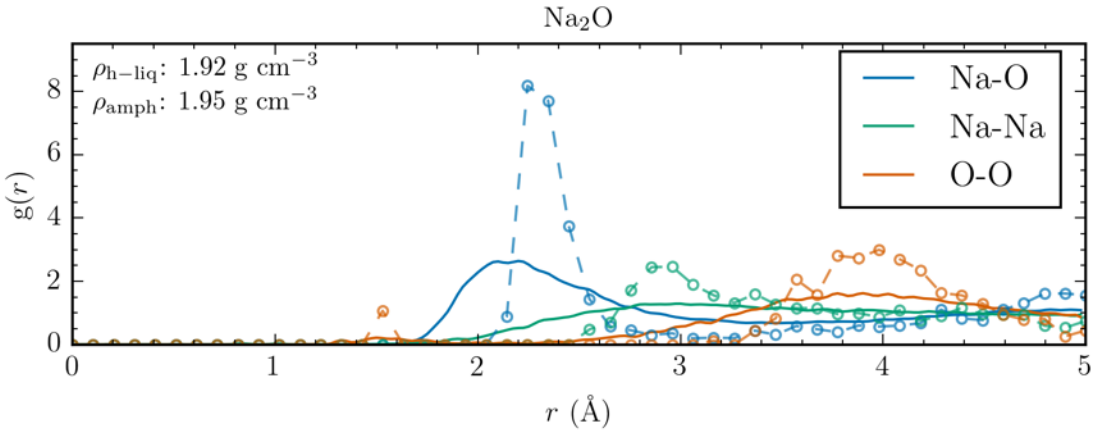

fig. S23. Radial distribution functions of amorphous configurations. Partial radial distribution functions of AIMD-generated amorphous Na_2O and the parent high-temperature hypothetical liquid that amorphous configurations are quenched from.

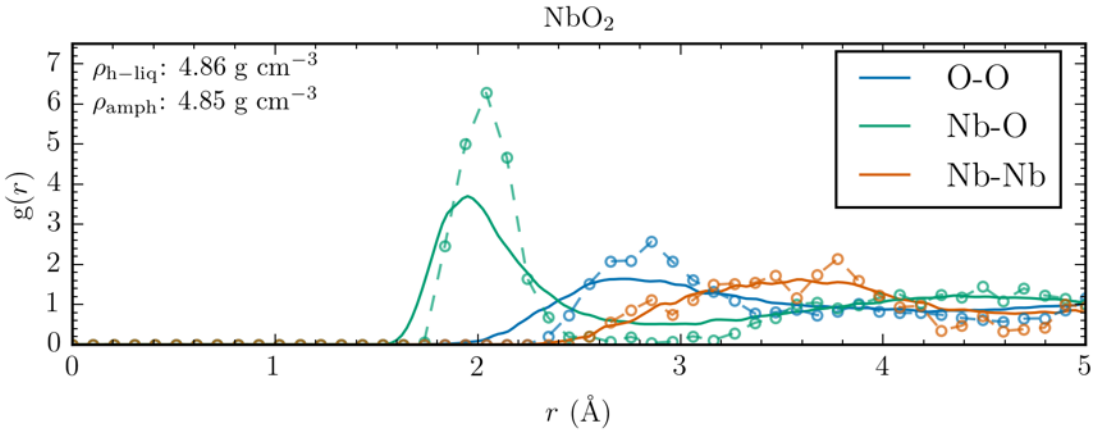

fig. S24. Radial distribution functions of amorphous configurations. Partial radial distribution functions of AIMD-generated amorphous NbO_2 and the parent high-temperature hypothetical liquid that amorphous configurations are quenched from.

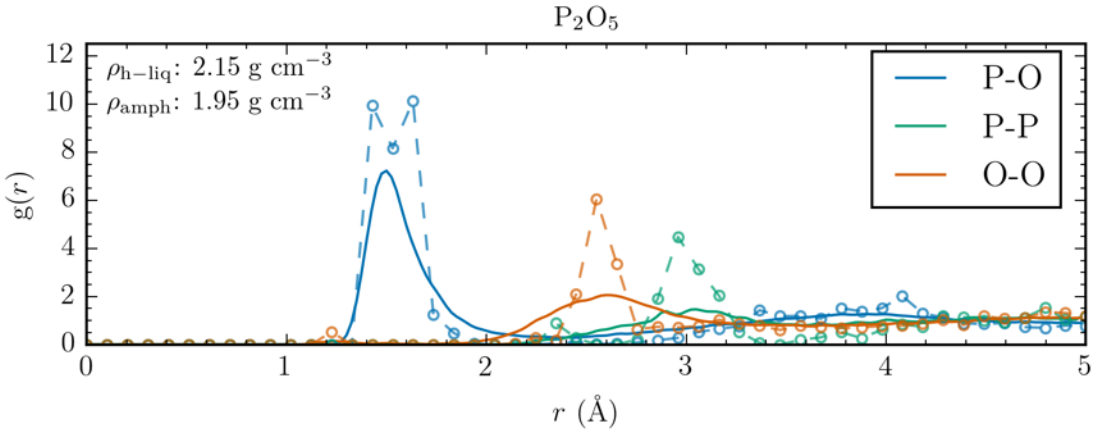

fig. S25. Radial distribution functions of amorphous configurations. Partial radial distribution functions of AIMD-generated amorphous P_2O_5 and the parent high-temperature hypothetical liquid that amorphous configurations are quenched from.

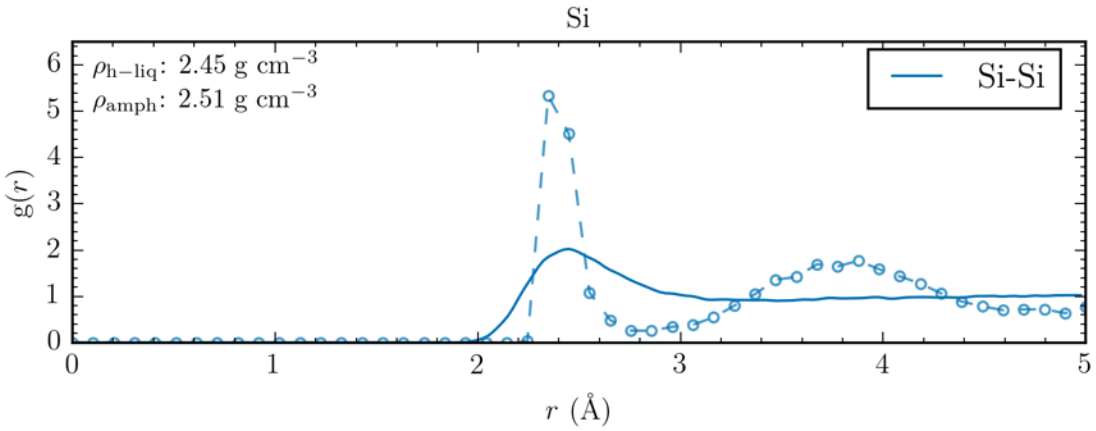

fig. S26. Radial distribution functions of amorphous configurations. Partial radial distribution functions of AIMD-generated amorphous Si and the parent high-temperature hypothetical liquid that amorphous configurations are quenched from.

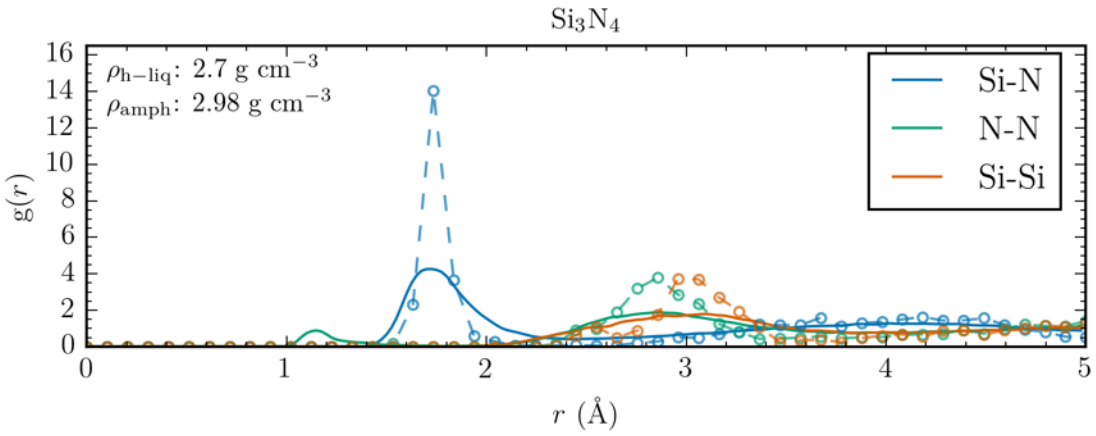

fig. S27. Radial distribution functions of amorphous configurations. Partial radial distribution functions of AIMD-generated amorphous Si_3N_4 and the parent high-temperature hypothetical liquid that amorphous configurations are quenched from.

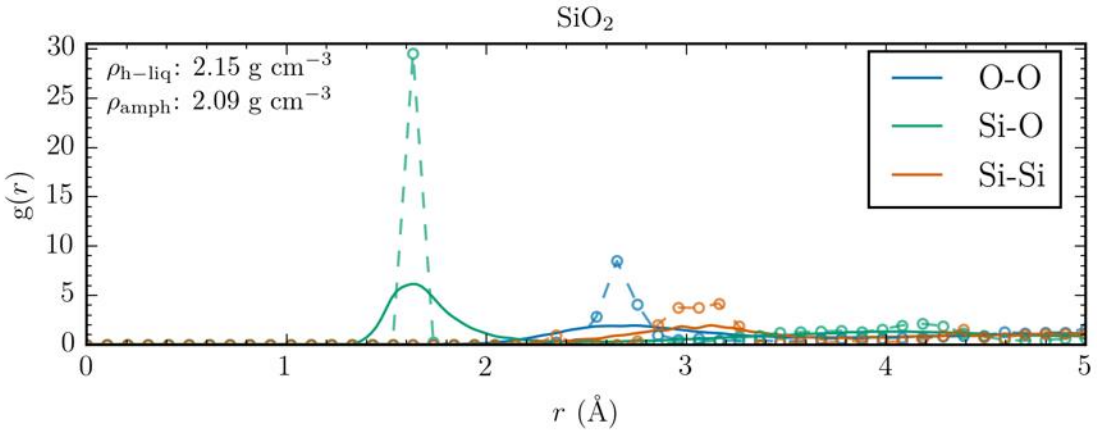

fig. S28. Radial distribution functions of amorphous configurations. Partial radial distribution functions of AIMD-generated amorphous SiO_2 and the parent high-temperature hypothetical liquid that amorphous configurations are quenched from.

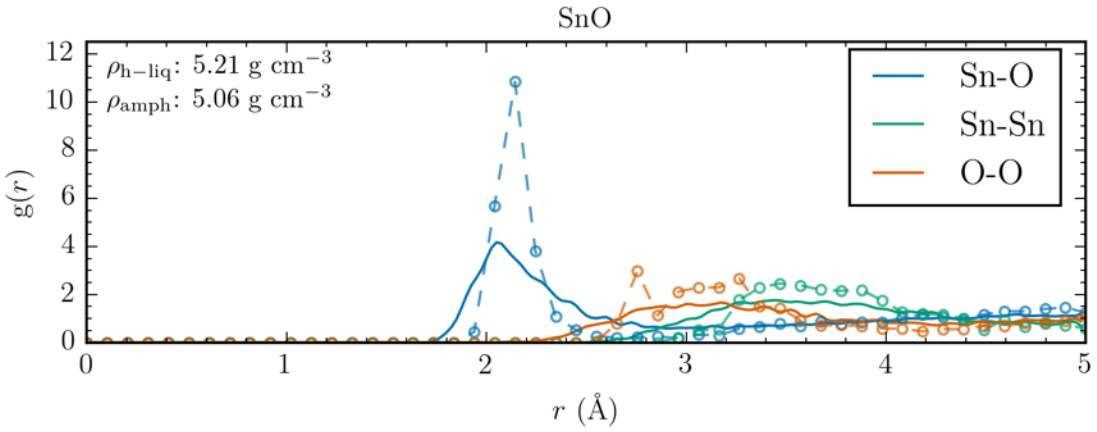

fig. S29. Radial distribution functions of amorphous configurations. Partial radial distribution functions of AIMD-generated amorphous SnO and the parent high-temperature hypothetical liquid that amorphous configurations are quenched from.

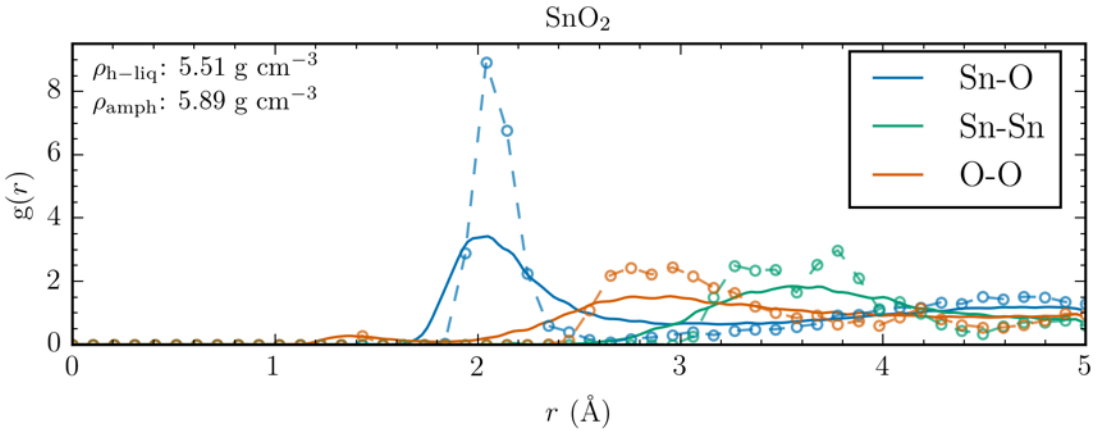

fig. S30. Radial distribution functions of amorphous configurations. Partial radial distribution functions of AIMD-generated amorphous SnO_2 and the parent high-temperature hypothetical liquid that amorphous configurations are quenched from.

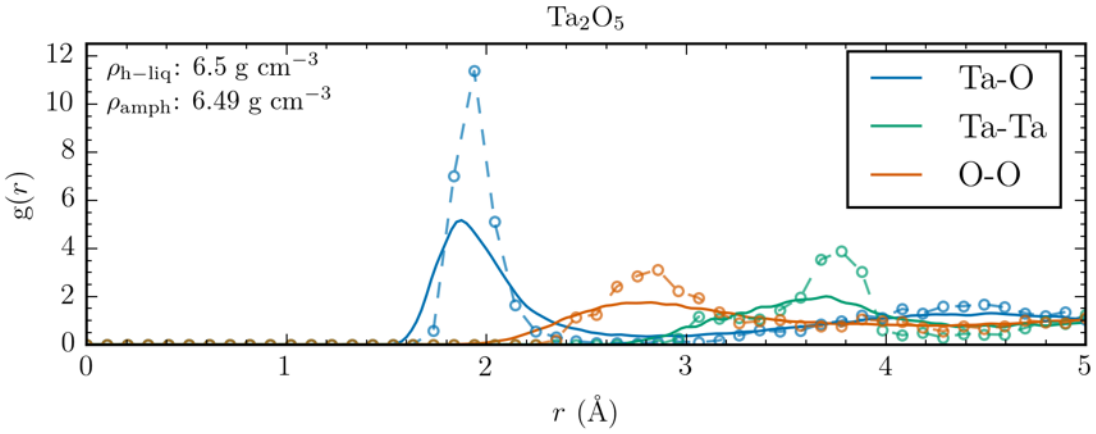

fig. S31. Radial distribution functions of amorphous configurations. Partial radial distribution functions of AIMD-generated amorphous Ta_2O_5 and the parent high-temperature hypothetical liquid that amorphous configurations are quenched from.

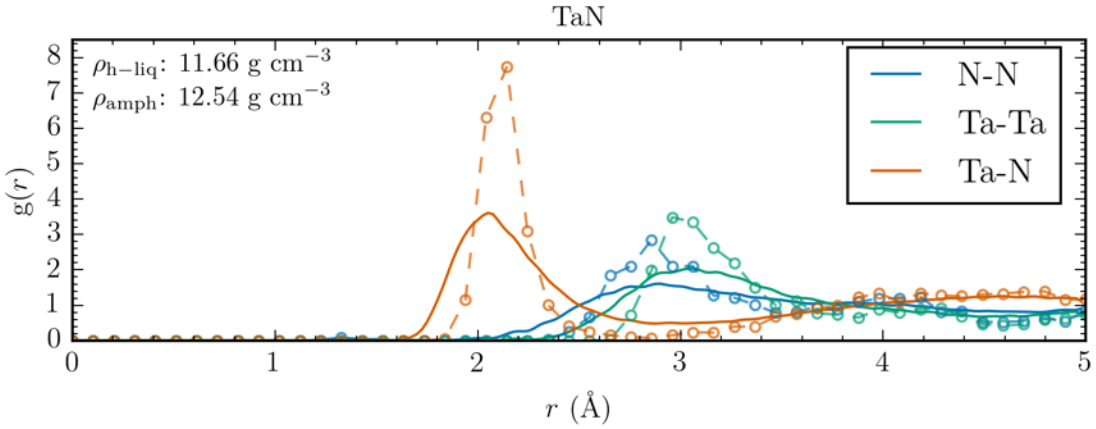

fig. S32. Radial distribution functions of amorphous configurations. Partial radial distribution functions of AIMD-generated amorphous TaN and the parent high-temperature hypothetical liquid that amorphous configurations are quenched from.

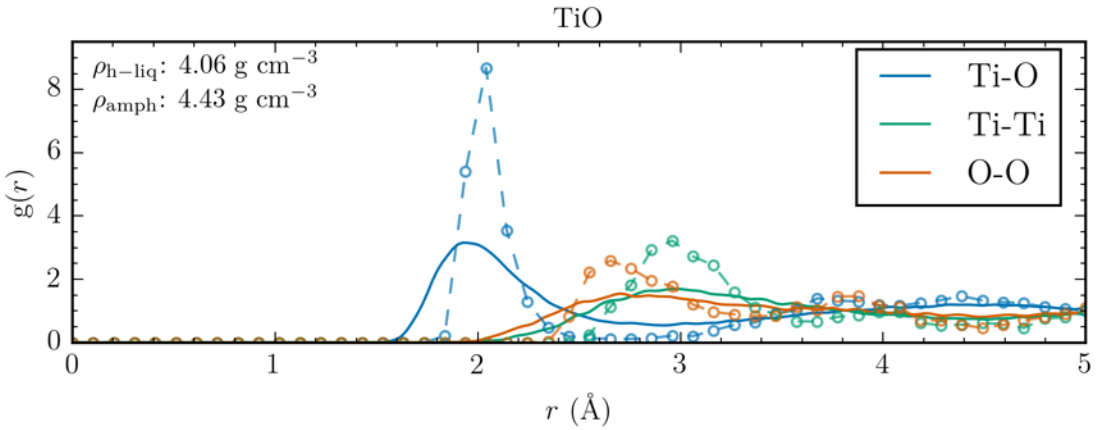

fig. S33. Radial distribution functions of amorphous configurations. Partial radial distribution functions of AIMD-generated amorphous TiO and the parent high-temperature hypothetical liquid that amorphous configurations are quenched from.

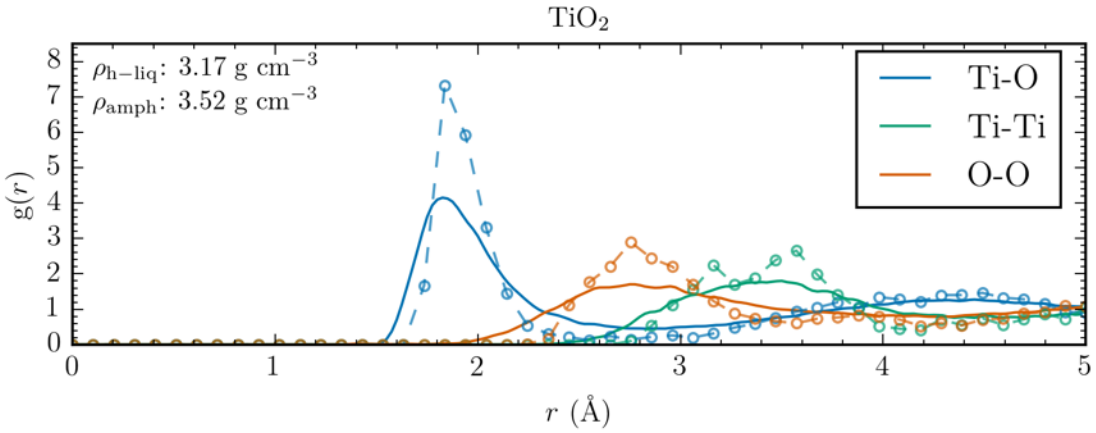

fig. S34. Radial distribution functions of amorphous configurations. Partial radial distribution functions of AIMD-generated amorphous TiO_2 and the parent high-temperature hypothetical liquid that amorphous configurations are quenched from.

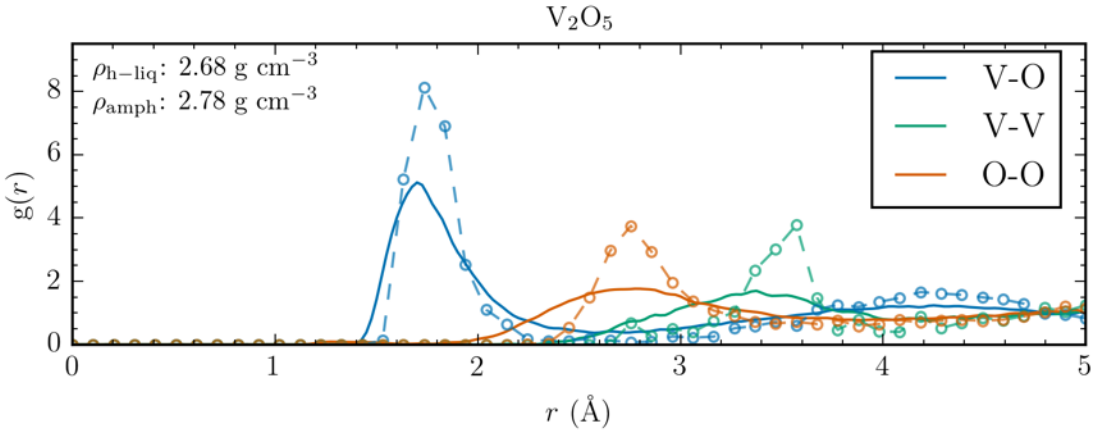

fig. S35. Radial distribution functions of amorphous configurations. Partial radial distribution functions of AIMD-generated amorphous V_2O_5 and the parent high-temperature hypothetical liquid that amorphous configurations are quenched from.

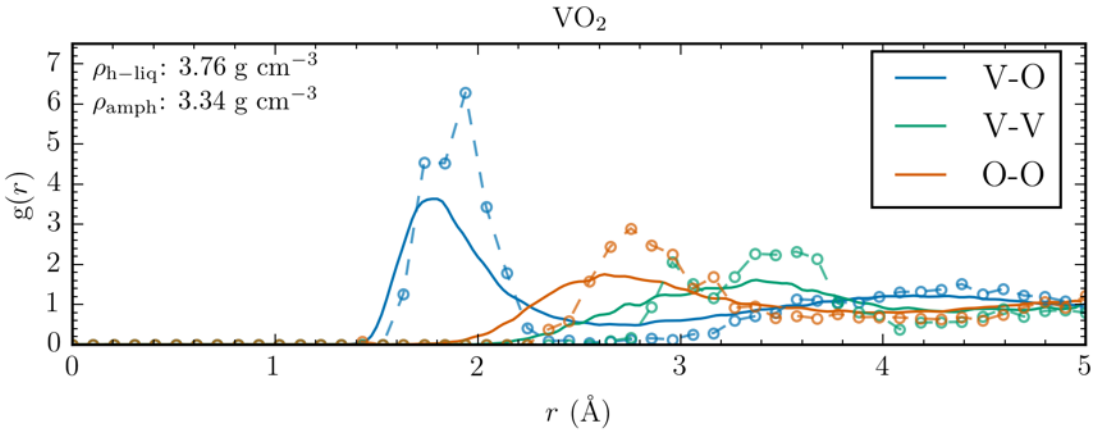

fig. S36. Radial distribution functions of amorphous configurations. Partial radial distribution functions of AIMD-generated amorphous VO_2 and the parent high-temperature hypothetical liquid that amorphous configurations are quenched from.

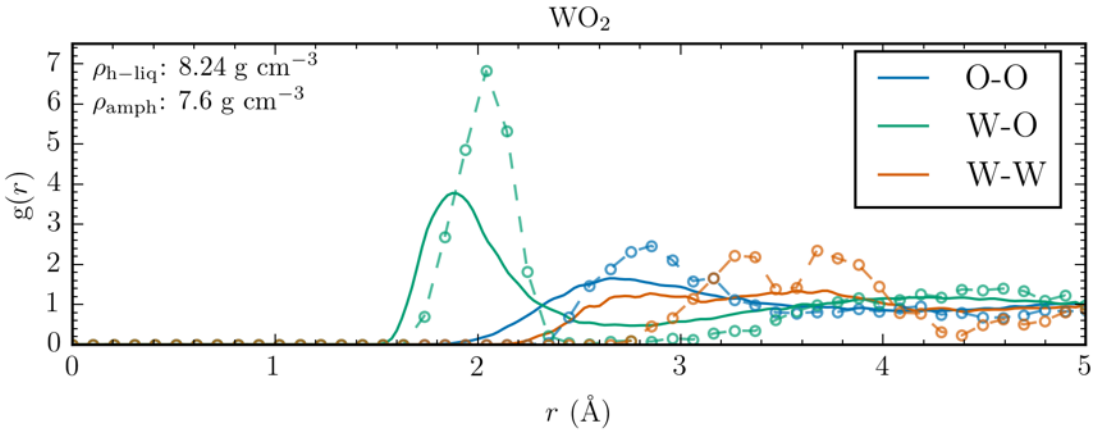

fig. S37. Radial distribution functions of amorphous configurations. Partial radial distribution functions of AIMD-generated amorphous WO_2 and the parent high-temperature hypothetical liquid that amorphous configurations are quenched from.

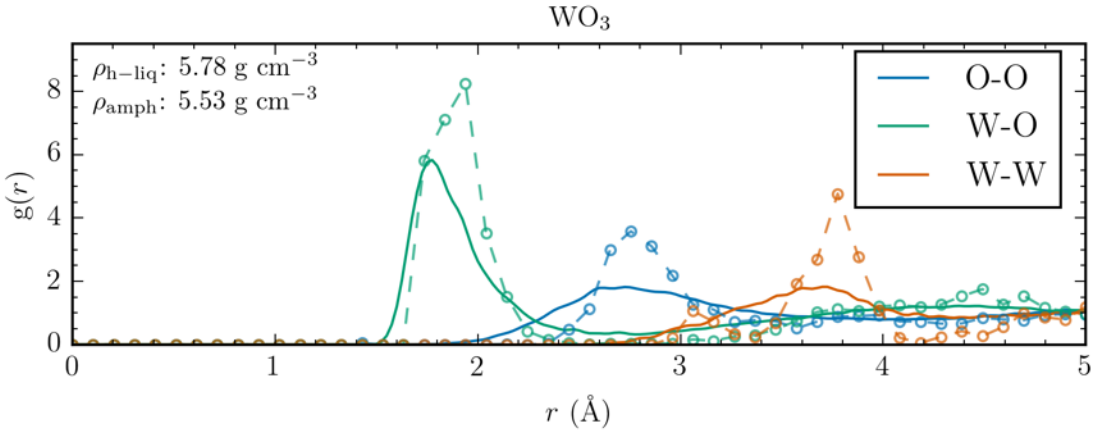

fig. S38. Radial distribution functions of amorphous configurations. Partial radial distribution functions of AIMD-generated amorphous WO_3 and the parent high-temperature hypothetical liquid that amorphous configurations are quenched from.

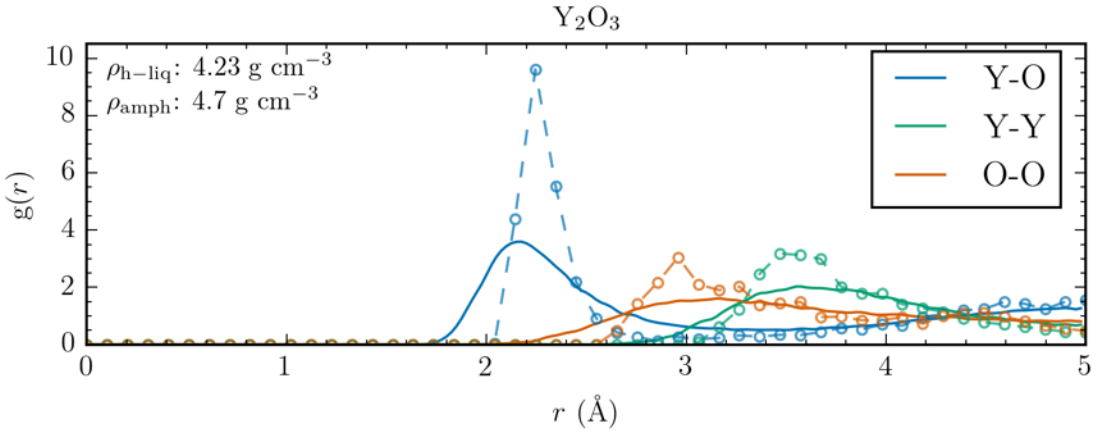

fig. S39. Radial distribution functions of amorphous configurations. Partial radial distribution functions of AIMD-generated amorphous Y_2O_3 and the parent high-temperature hypothetical liquid that amorphous configurations are quenched from.

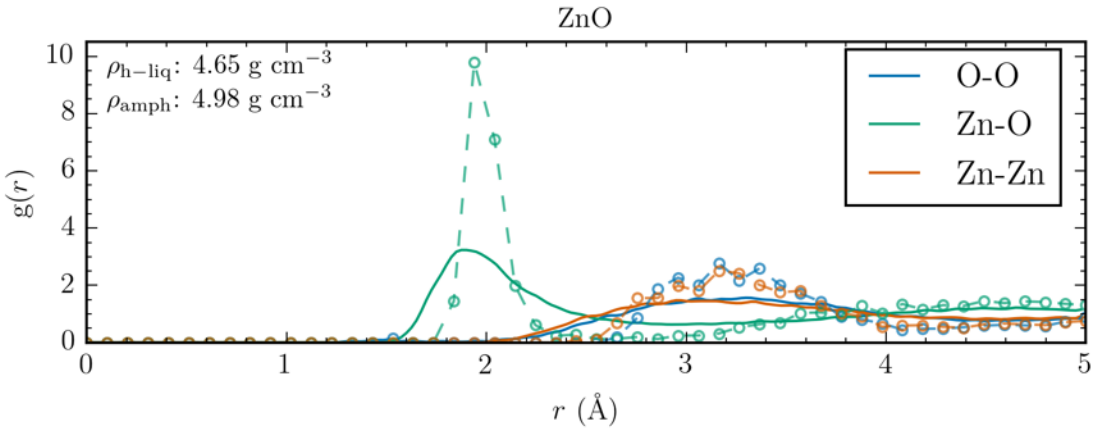

fig. S40. Radial distribution functions of amorphous configurations. Partial radial distribution functions of AIMD-generated amorphous ZnO and the parent high-temperature hypothetical liquid that amorphous configurations are quenched from.

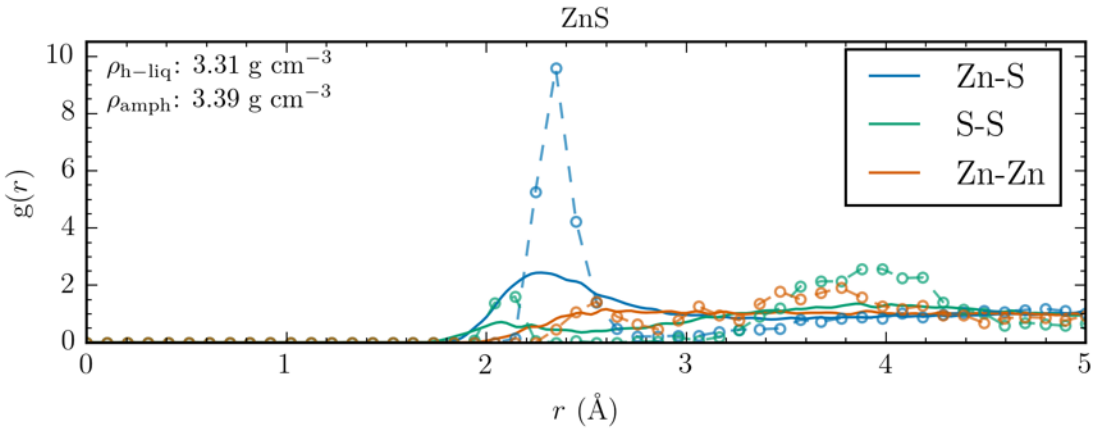

fig. S41. Radial distribution functions of amorphous configurations. Partial radial distribution functions of AIMD-generated amorphous ZnS and the parent high-temperature hypothetical liquid that amorphous configurations are quenched from.

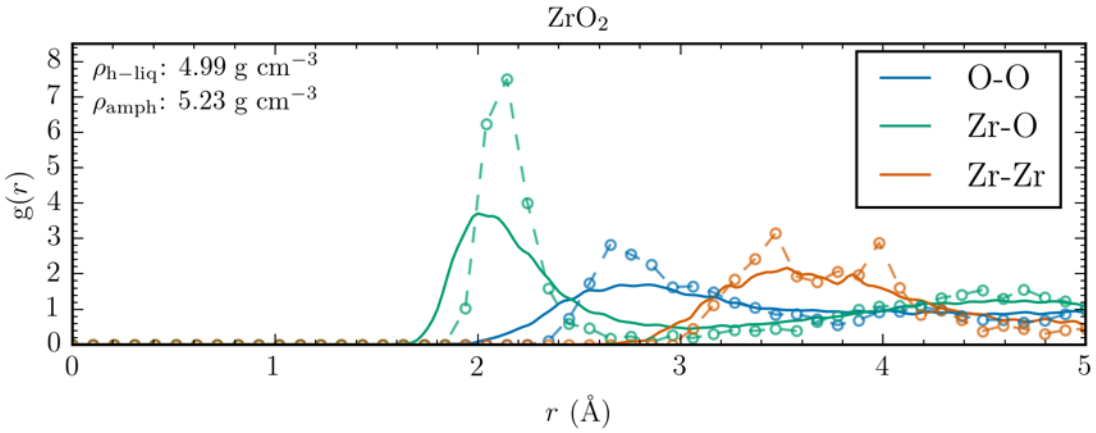

fig. S42. Radial distribution functions of amorphous configurations. Partial radial distribution functions of AIMD-generated amorphous ZrO_2 and the parent high-temperature hypothetical liquid that amorphous configurations are quenched from.

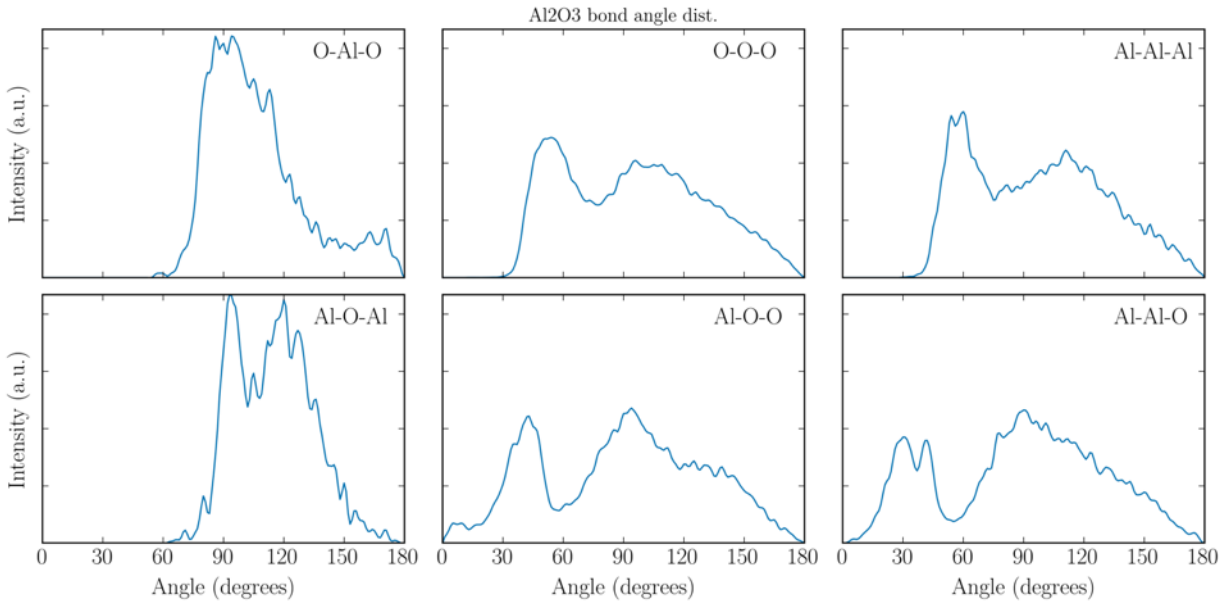

fig. S43. Bond-angle distribution functions of amorphous configurations. Bond angle distribution functions of AIMD-generated amorphous Al_2O_3.

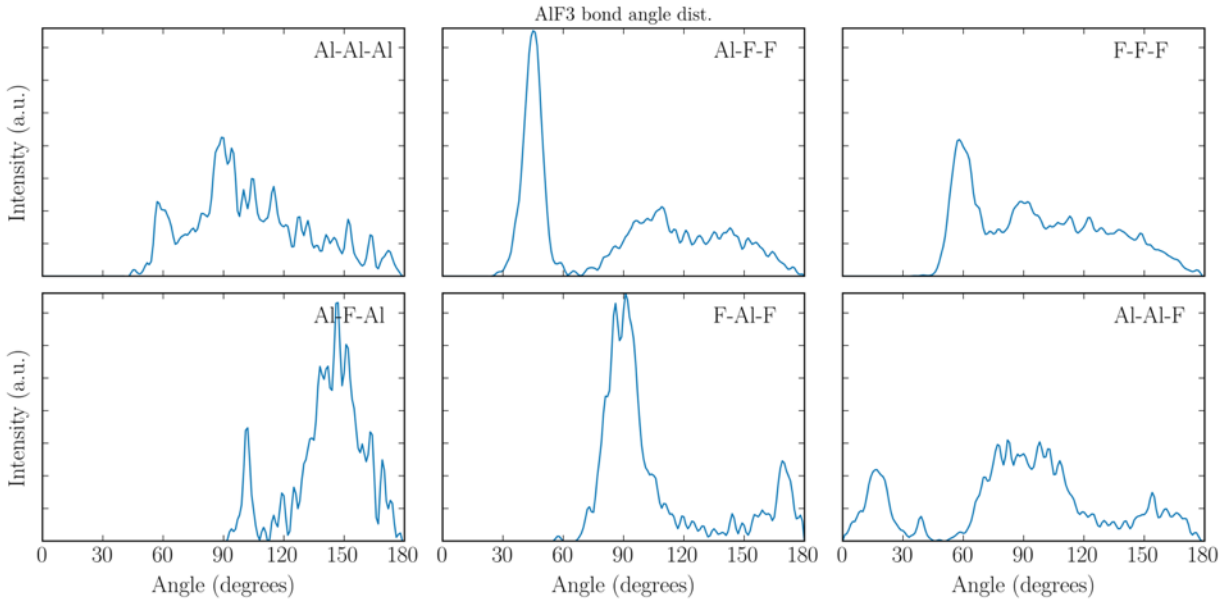

fig. S44. Bond-angle distribution functions of amorphous configurations. Bond angle distribution functions of AIMD-generated amorphous AlF_3.

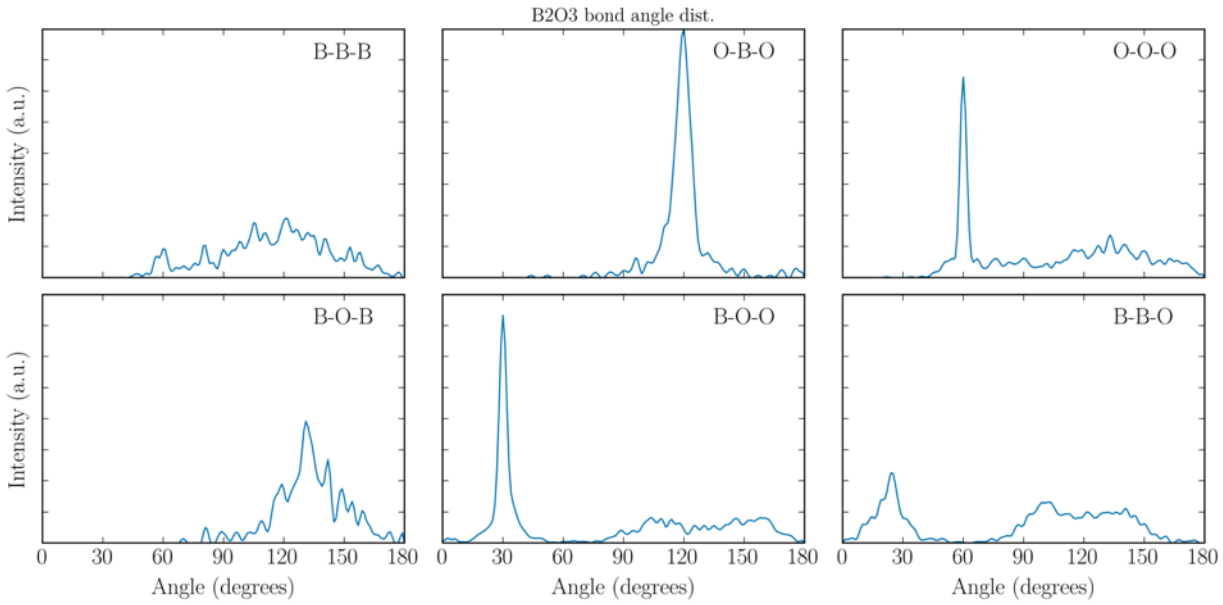

fig. S45. Bond-angle distribution functions of amorphous configurations. Bond angle distribution functions of AIMD-generated amorphous B_2O_3.

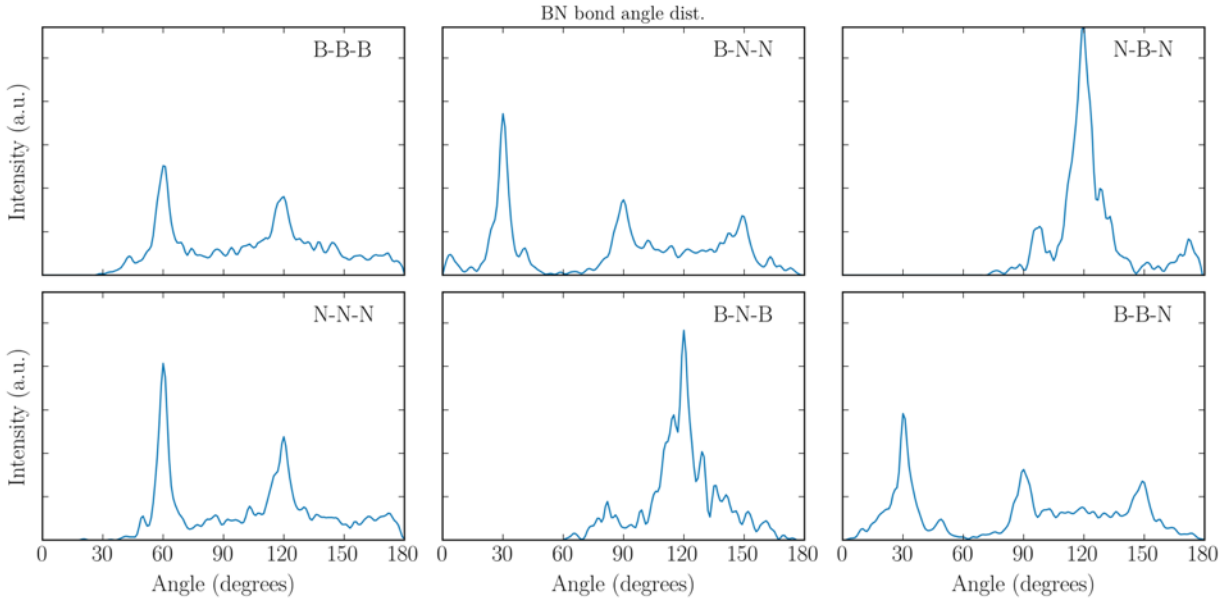

fig. S46. Bond-angle distribution functions of amorphous configurations. Bond angle distribution functions of AIMD-generated amorphous BN.

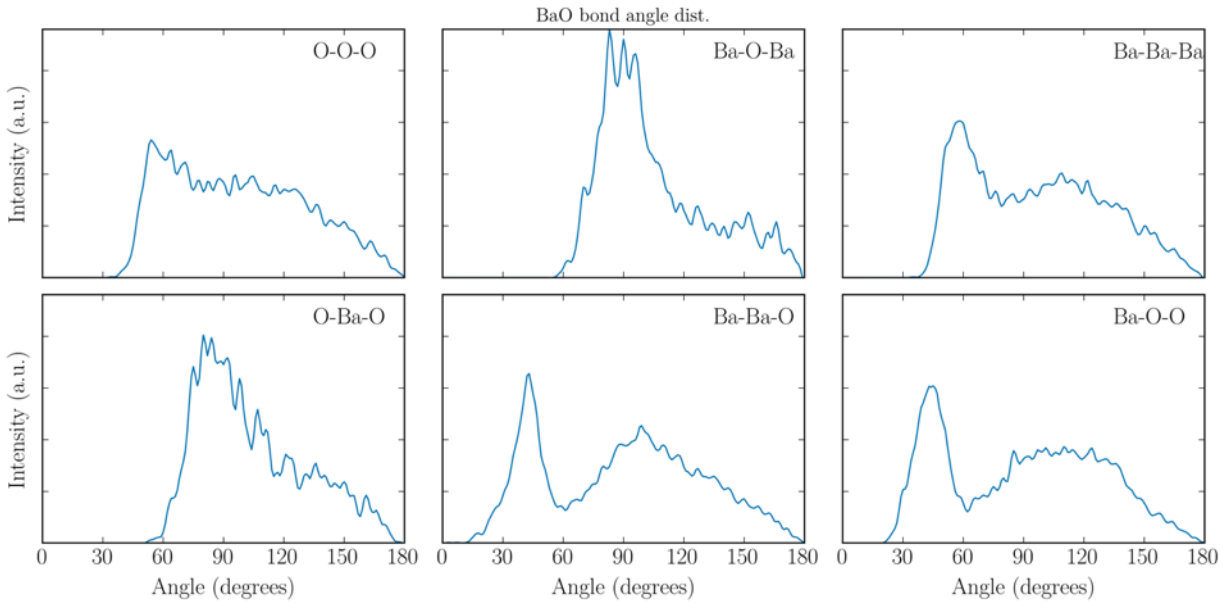

fig. S47. Bond-angle distribution functions of amorphous configurations. Bond angle distribution functions of AIMD-generated amorphous BaO.

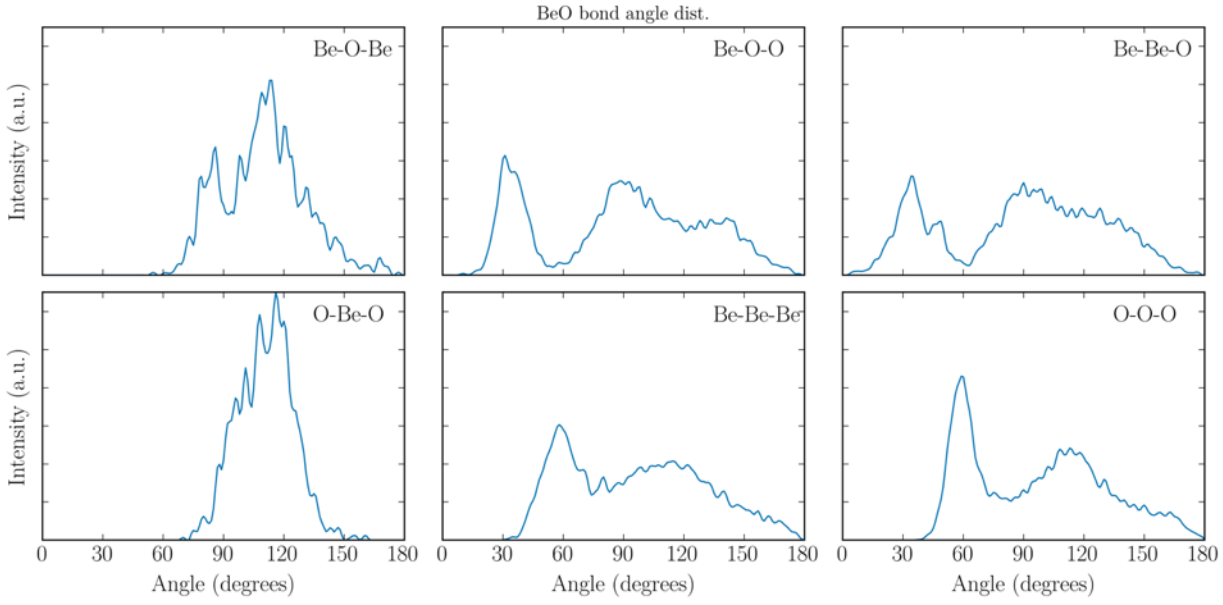

fig. S48. Bond-angle distribution functions of amorphous configurations. Bond angle distribution functions of AIMD-generated amorphous BeO.

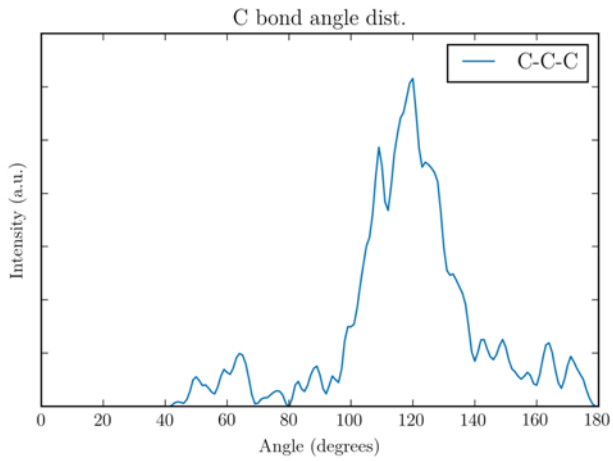

fig. S49. Bond-angle distribution functions of amorphous configurations. Bond angle distribution function of AIMD-generated amorphous C.

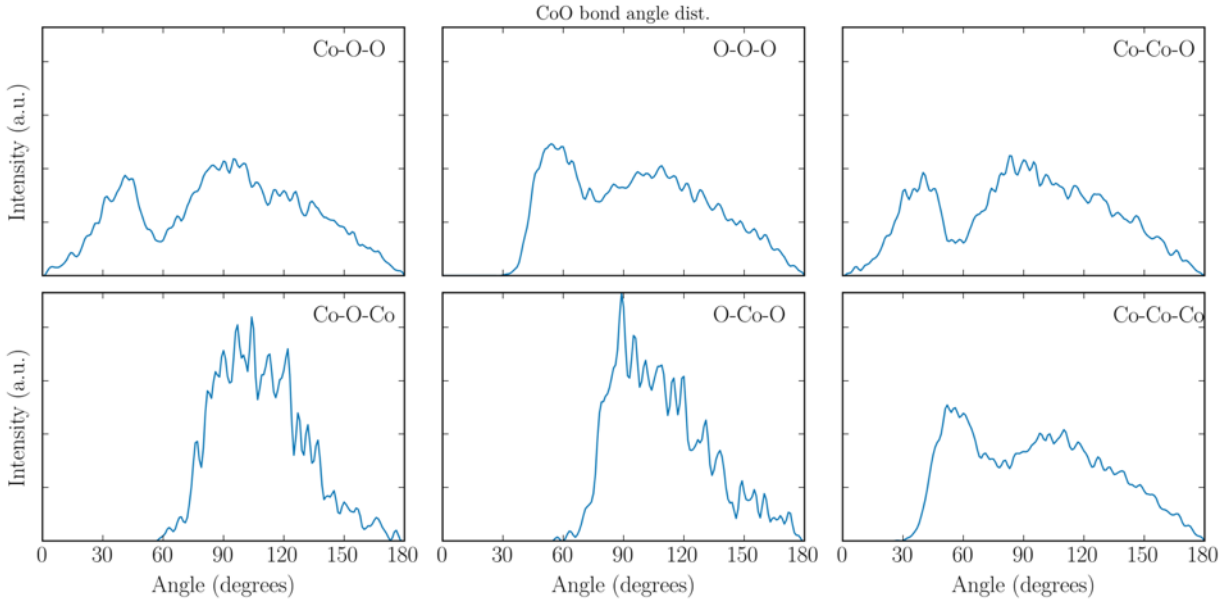

fig. S50. Bond-angle distribution functions of amorphous configurations. Bond angle distribution functions of AIMD-generated amorphous CoO.

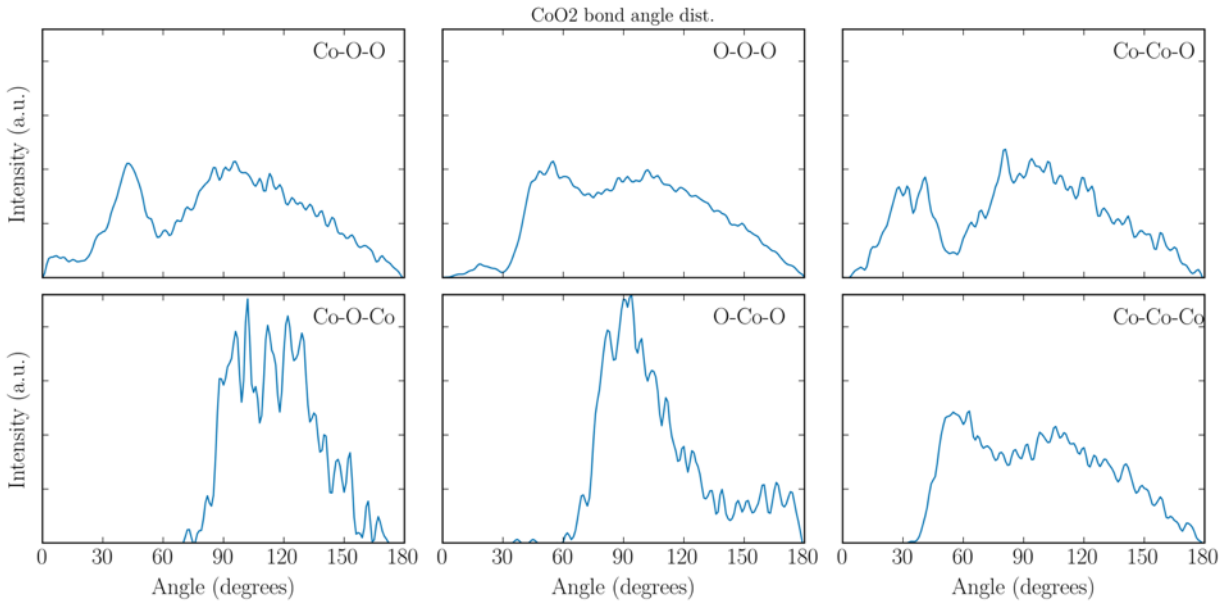

fig. S51. Bond-angle distribution functions of amorphous configurations. Bond angle distribution functions of AIMD-generated amorphous CoO_2.

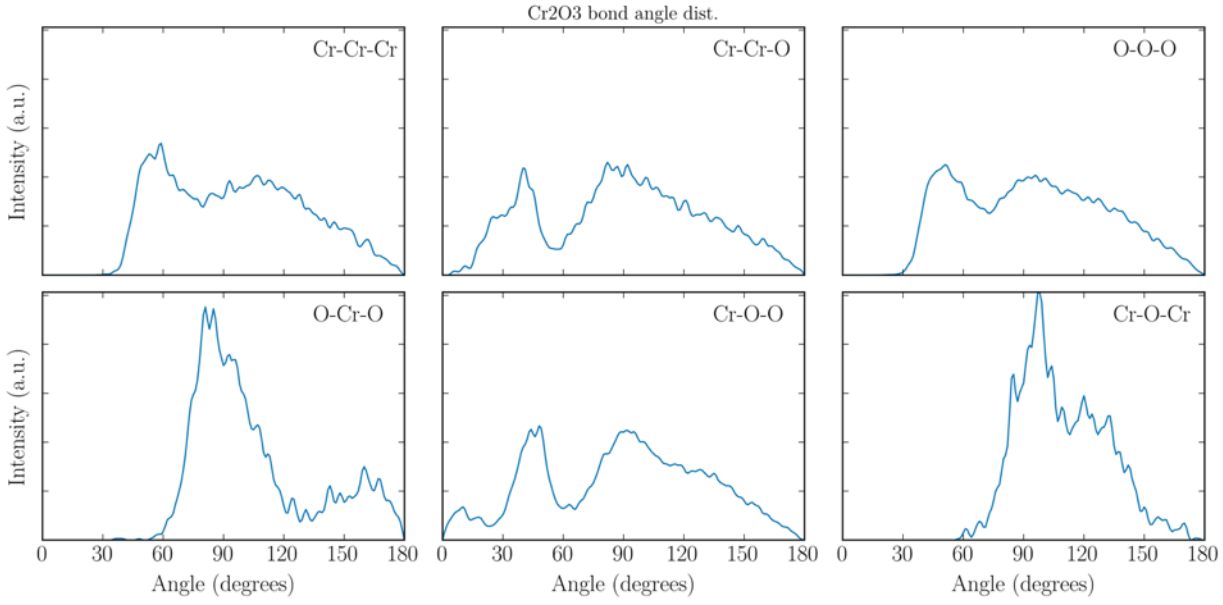

fig. S52. Bond-angle distribution functions of amorphous configurations. Bond angle distribution functions of AIMD-generated amorphous Cr_2O_3.

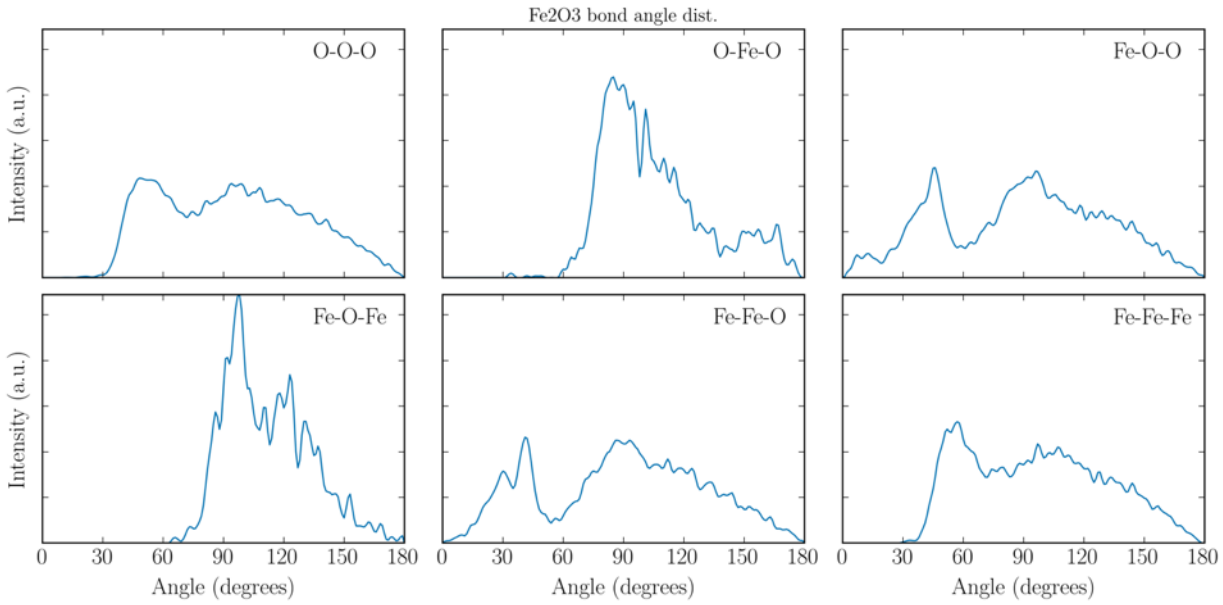

fig. S53. Bond-angle distribution functions of amorphous configurations. Bond angle distribution functions of AIMD-generated amorphous Fe_2O_3.

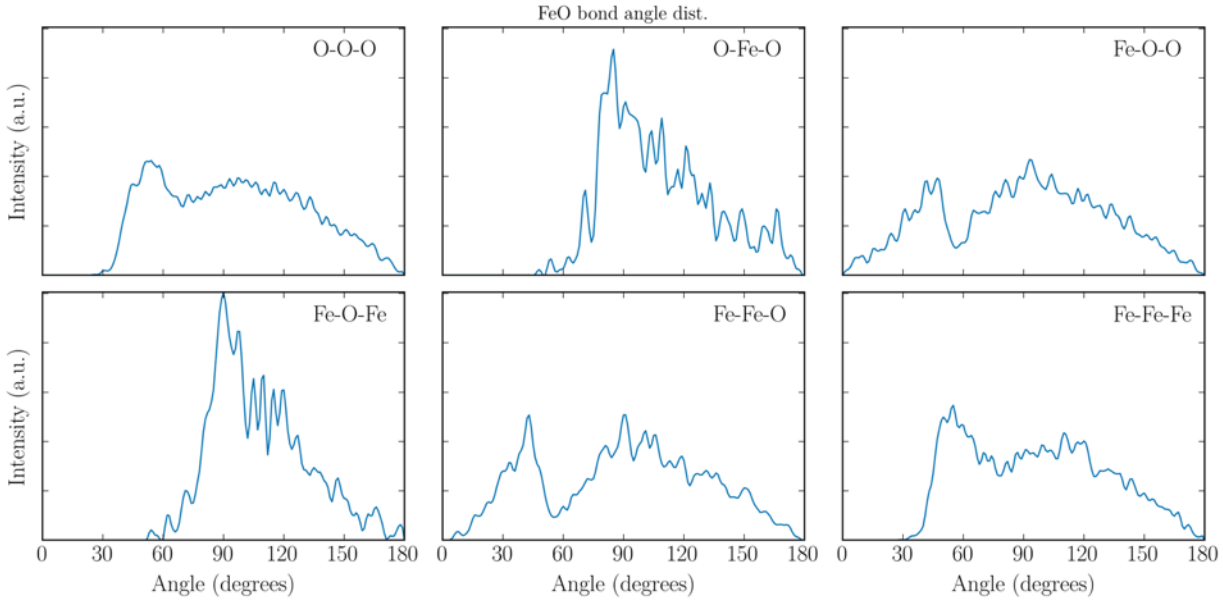

fig. S54. Bond-angle distribution functions of amorphous configurations. Bond angle distribution functions of AIMD-generated amorphous FeO.

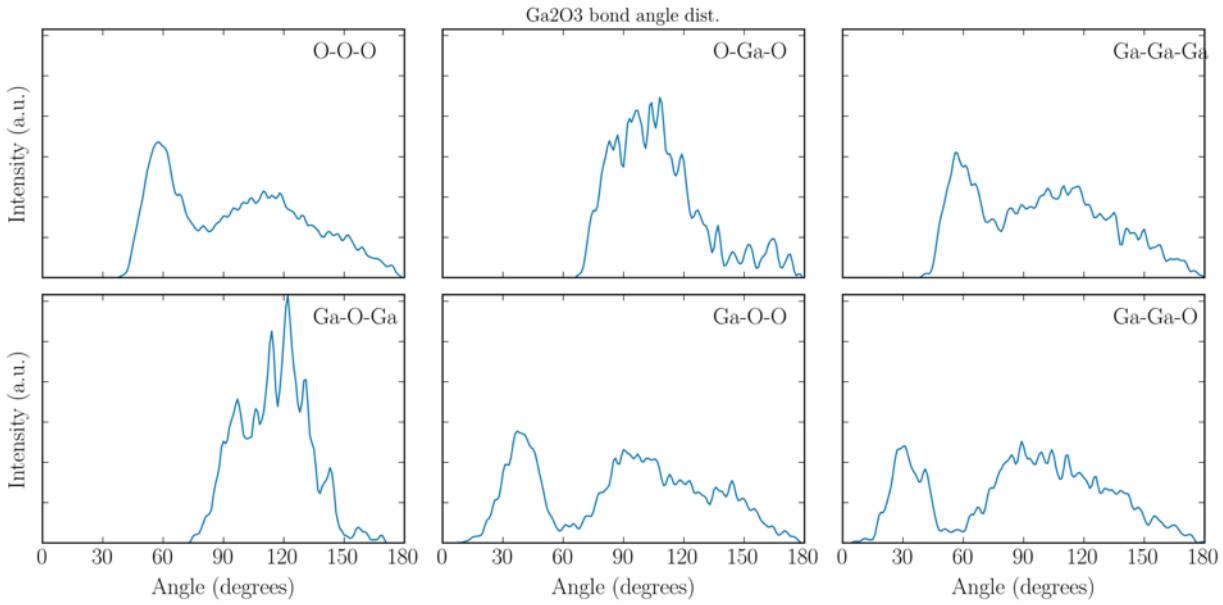

fig. S55. Bond-angle distribution functions of amorphous configurations. Bond angle distribution functions of AIMD-generated amorphous Ga_2O_3.

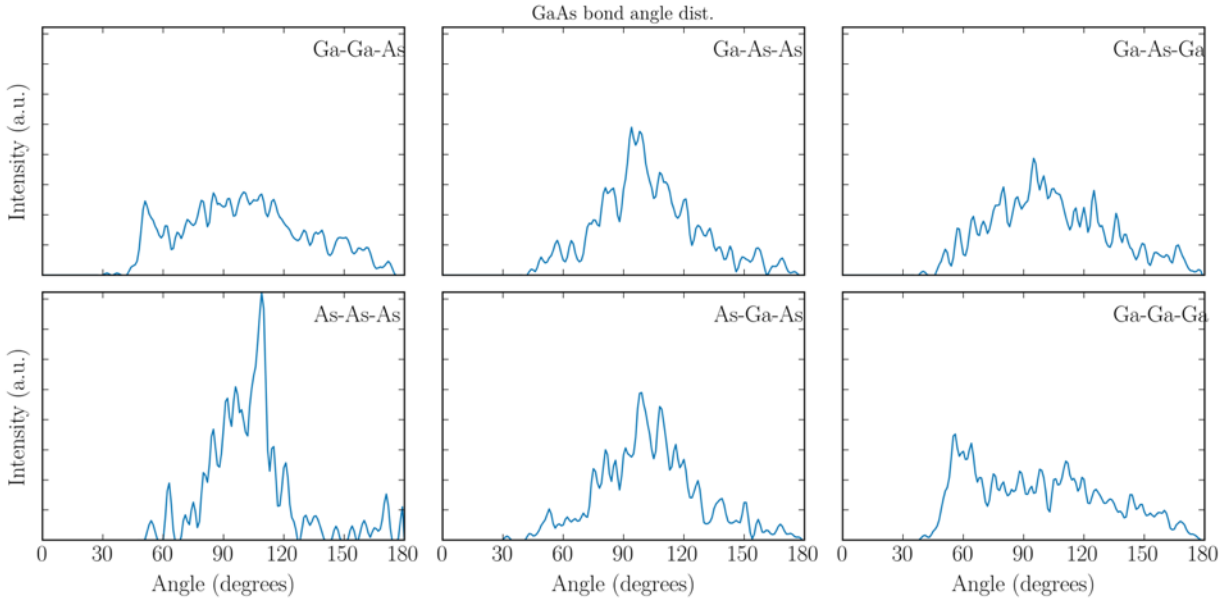

fig. S56. Bond-angle distribution functions of amorphous configurations. Bond angle distribution functions of AIMD-generated amorphous GaAs.

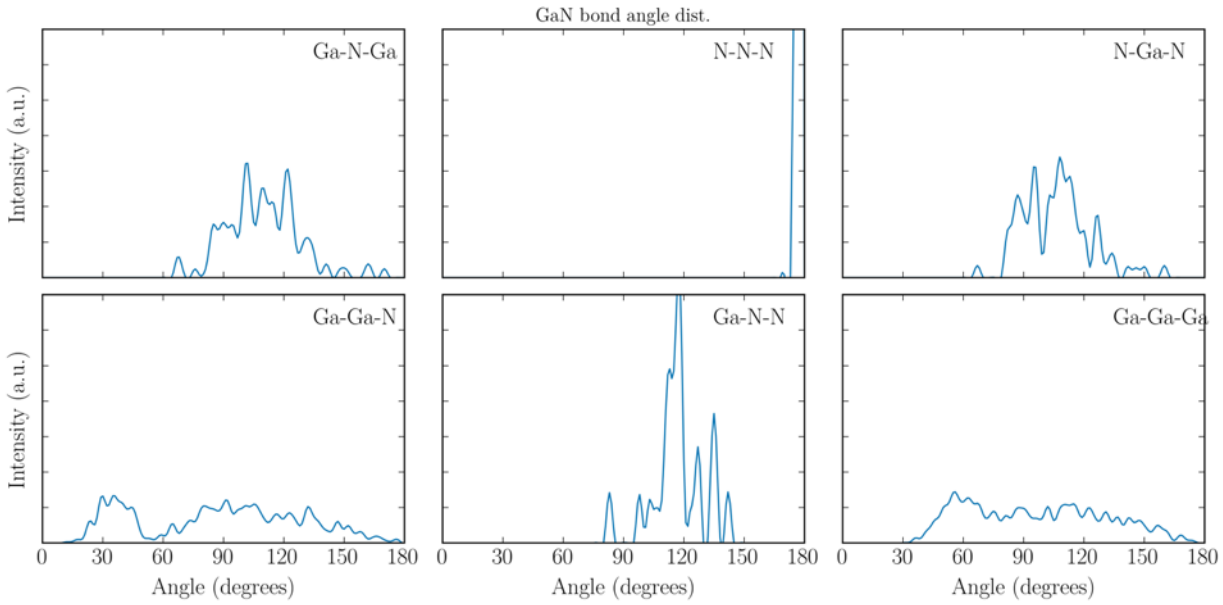

fig. S57. Bond-angle distribution functions of amorphous configurations. Bond angle distribution functions of AIMD-generated amorphous GaN.

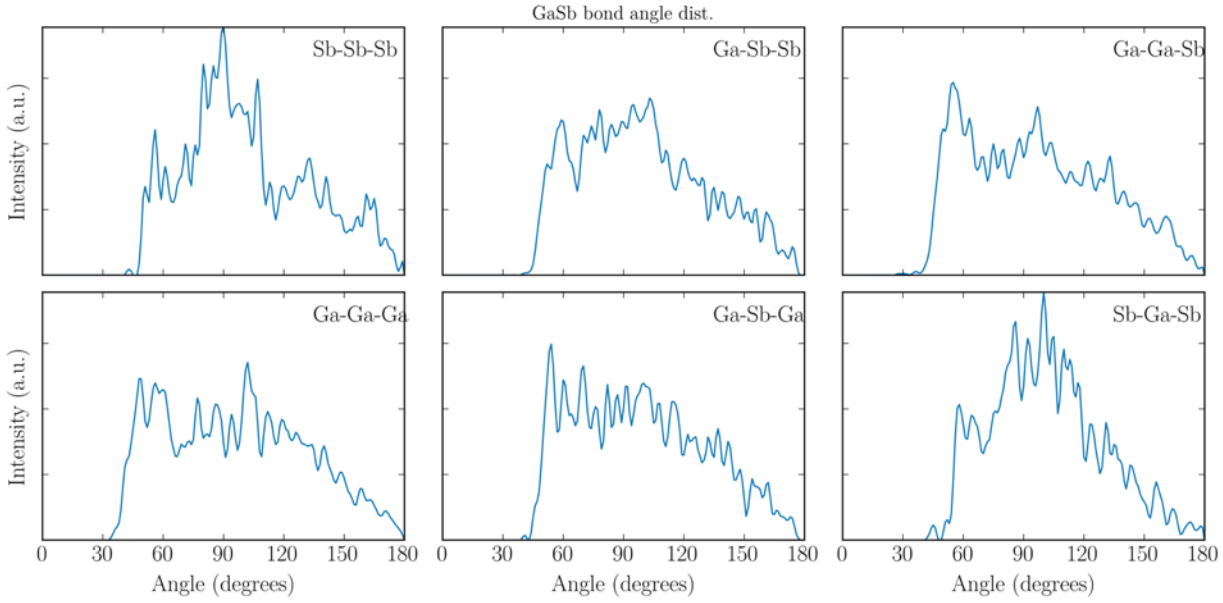

fig. S58. Bond-angle distribution functions of amorphous configurations. Bond angle distribution functions of AIMD-generated amorphous GaSb.

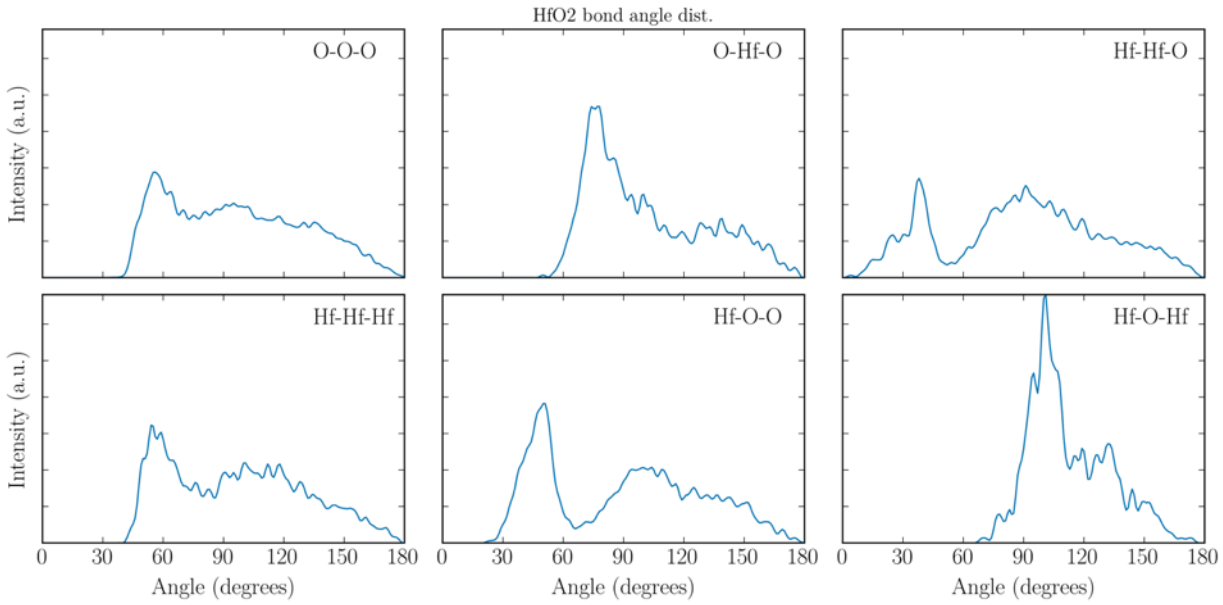

fig. S59. Bond-angle distribution functions of amorphous configurations. Bond angle distribution functions of AIMD-generated amorphous HfO_2.

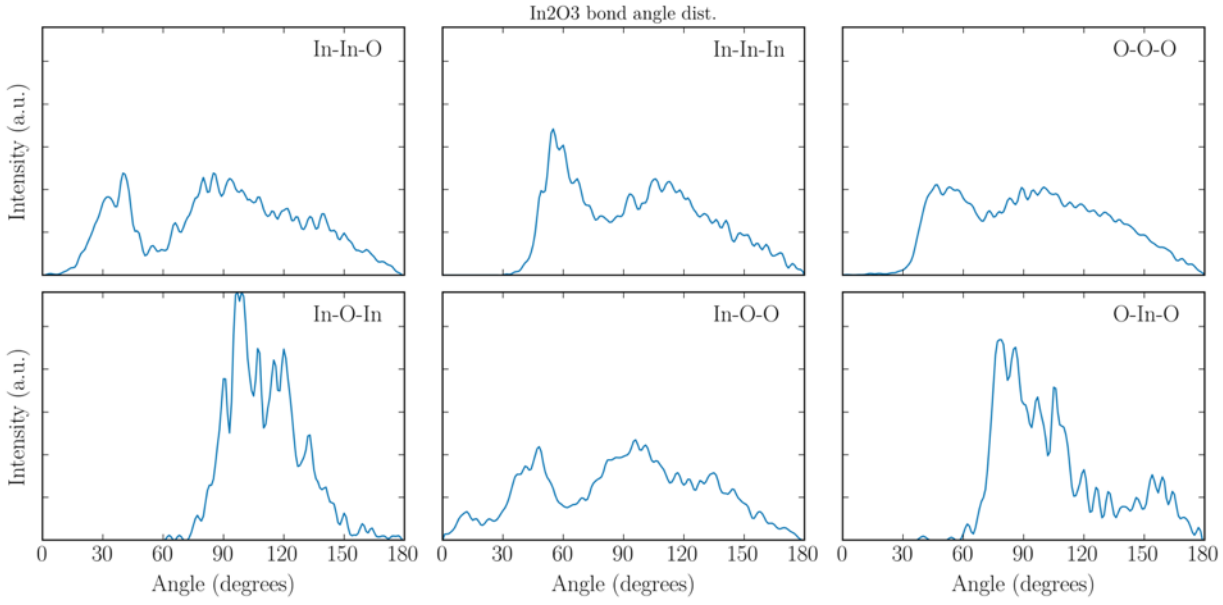

fig. S60. Bond-angle distribution functions of amorphous configurations. Bond angle distribution functions of AIMD-generated amorphous In_2O_3.

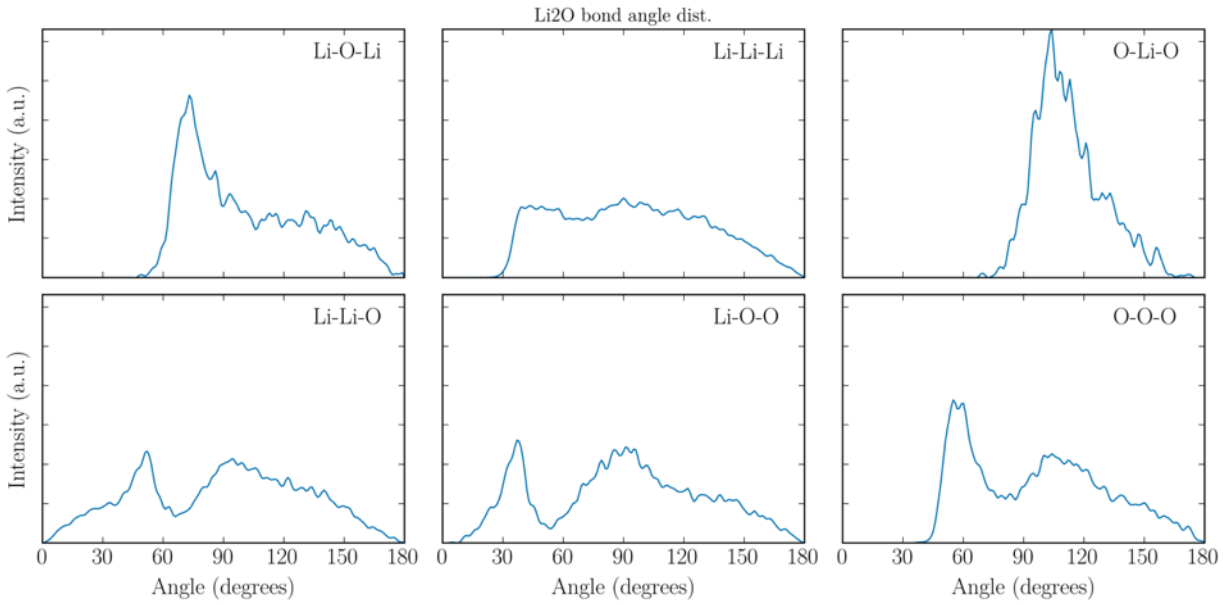

fig. S61. Bond-angle distribution functions of amorphous configurations. Bond angle distribution functions of AIMD-generated amorphous Li_2O.

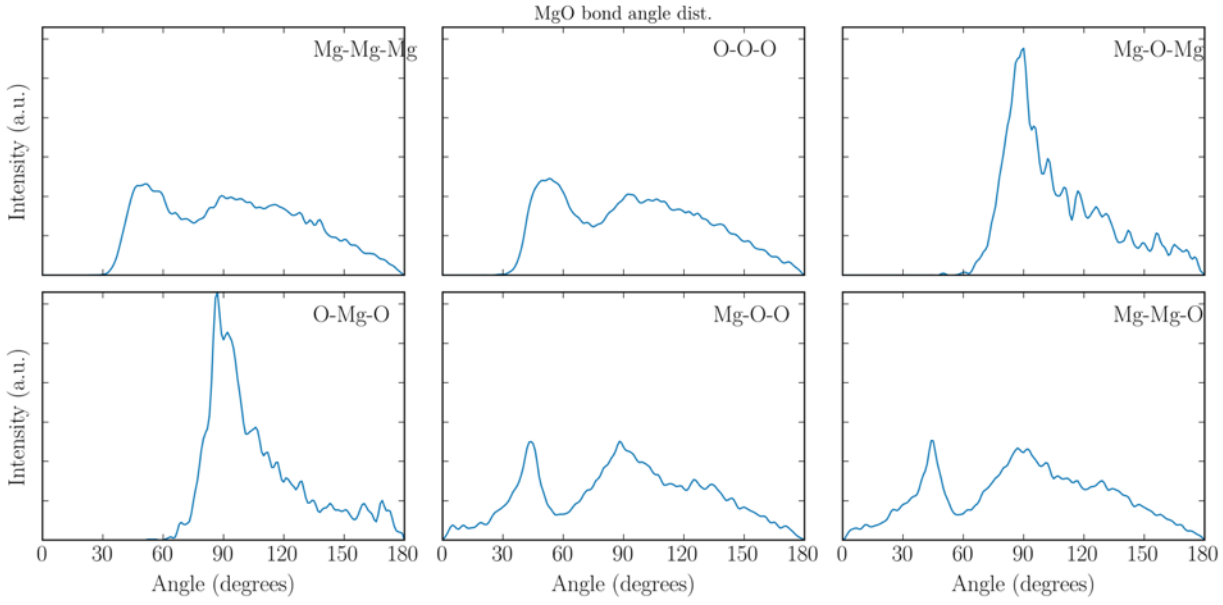

fig. S62. Bond-angle distribution functions of amorphous configurations. Bond angle distribution functions of AIMD-generated amorphous MgO.

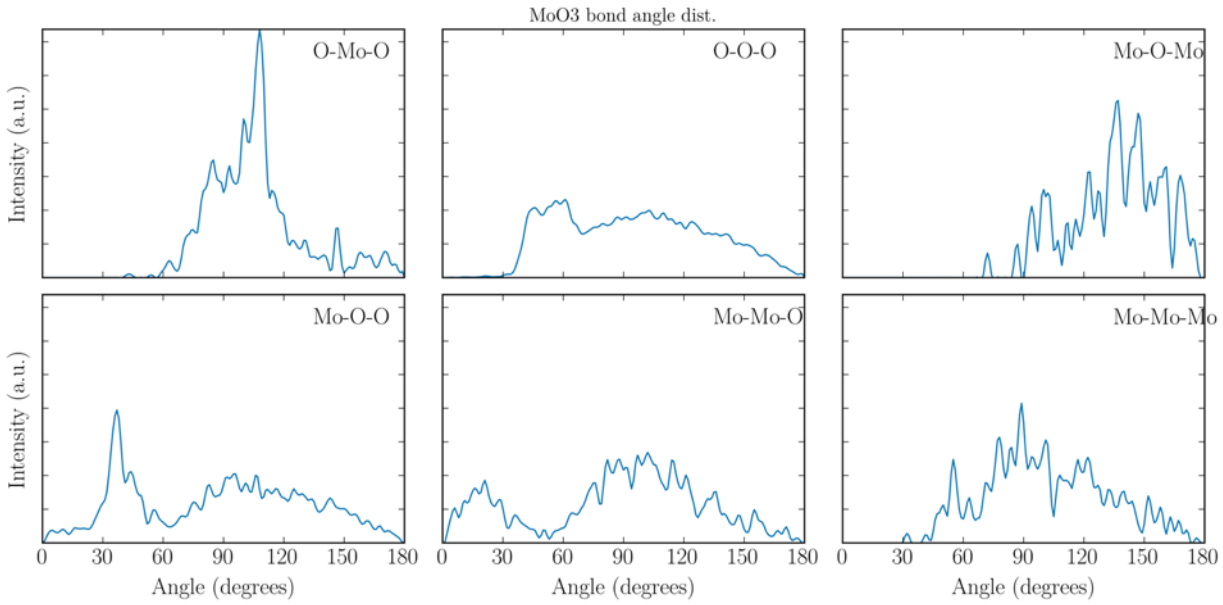

fig. S63. Bond-angle distribution functions of amorphous configurations. Bond angle distribution functions of AIMD-generated amorphous MoO_3.

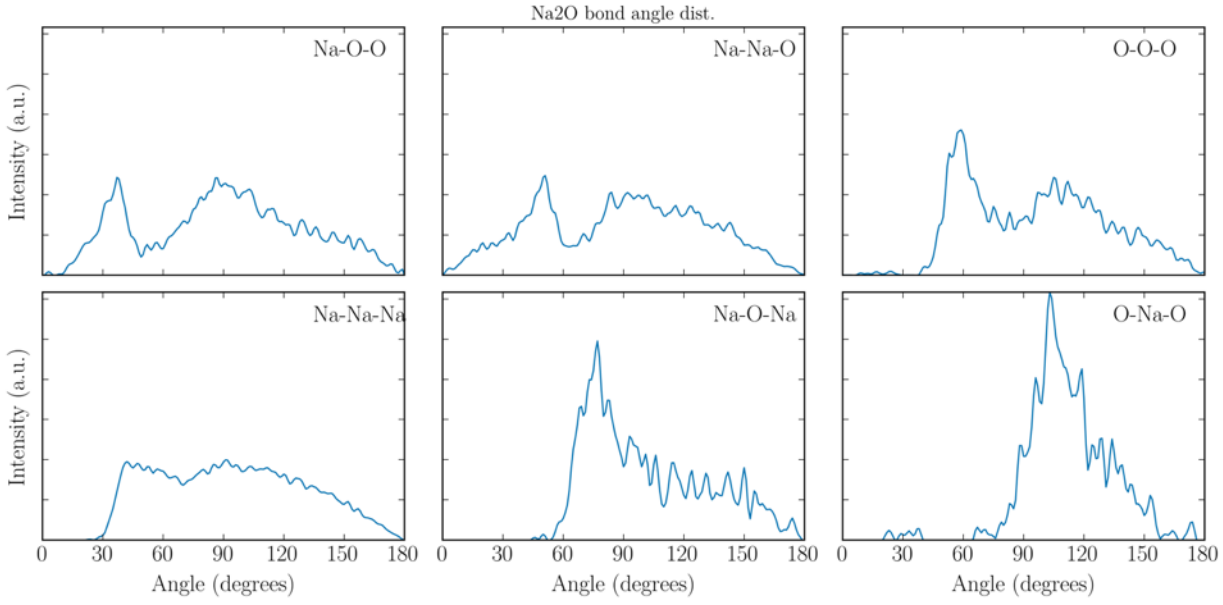

fig. S64. Bond-angle distribution functions of amorphous configurations. Bond angle distribution functions of AIMD-generated amorphous Na_2O.

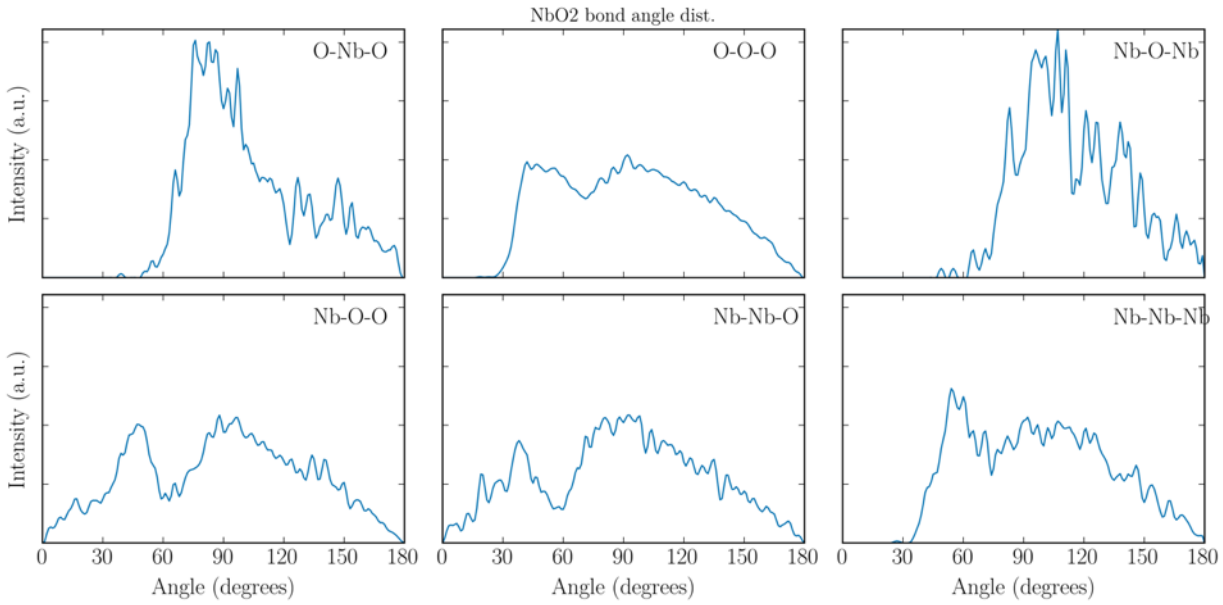

fig. S65. Bond-angle distribution functions of amorphous configurations. Bond angle distribution functions of AIMD-generated amorphous NbO_2.

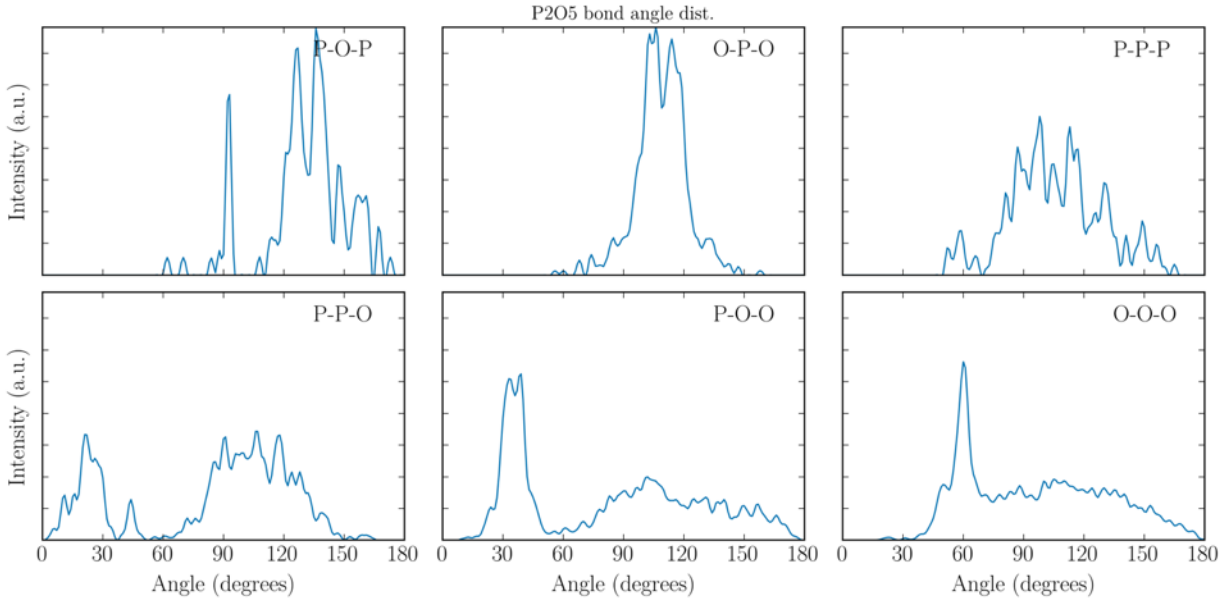

fig. S66. Bond-angle distribution functions of amorphous configurations. Bond angle distribution functions of AIMD-generated amorphous P_2O_5.

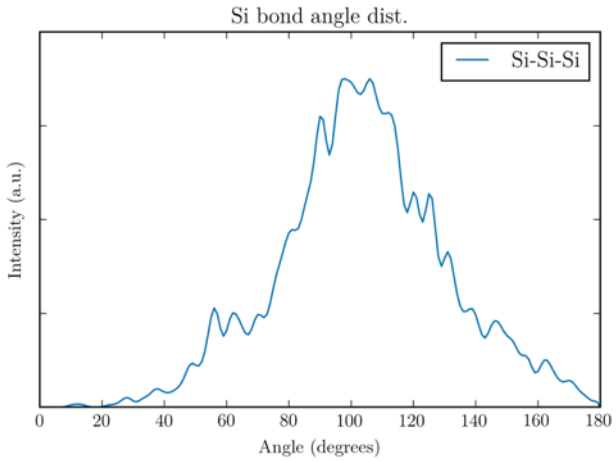

fig. S67. Bond-angle distribution functions of amorphous configurations. Bond angle distribution function of AIMD-generated amorphous Si.

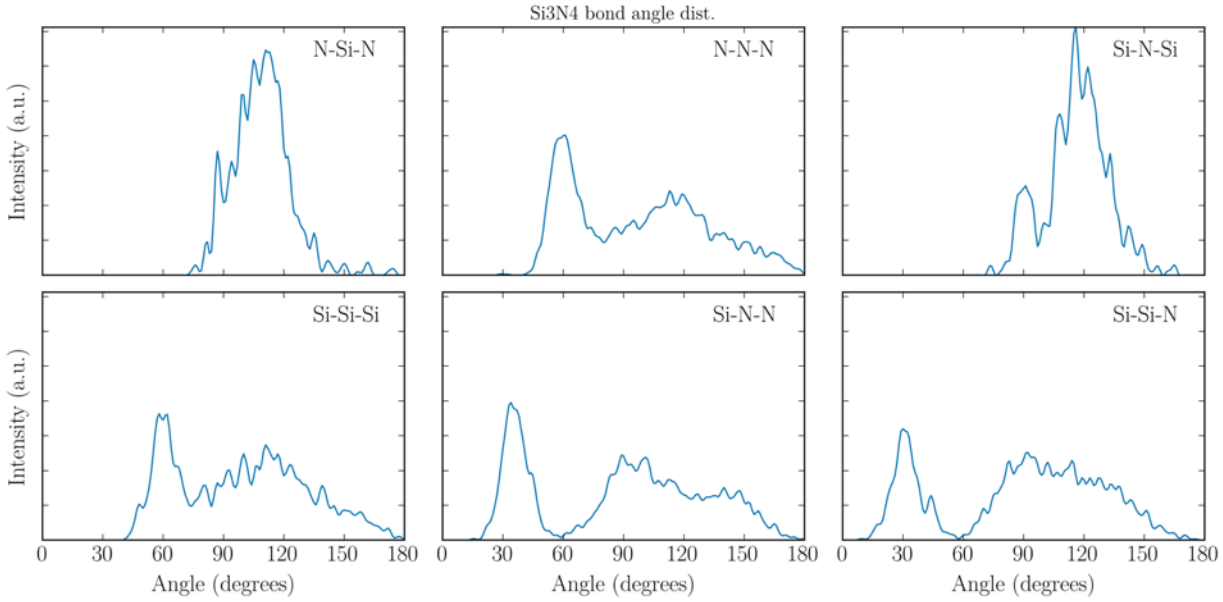

fig. S68. Bond-angle distribution functions of amorphous configurations. Bond angle distribution functions of AIMD-generated amorphous Si_3N_4.

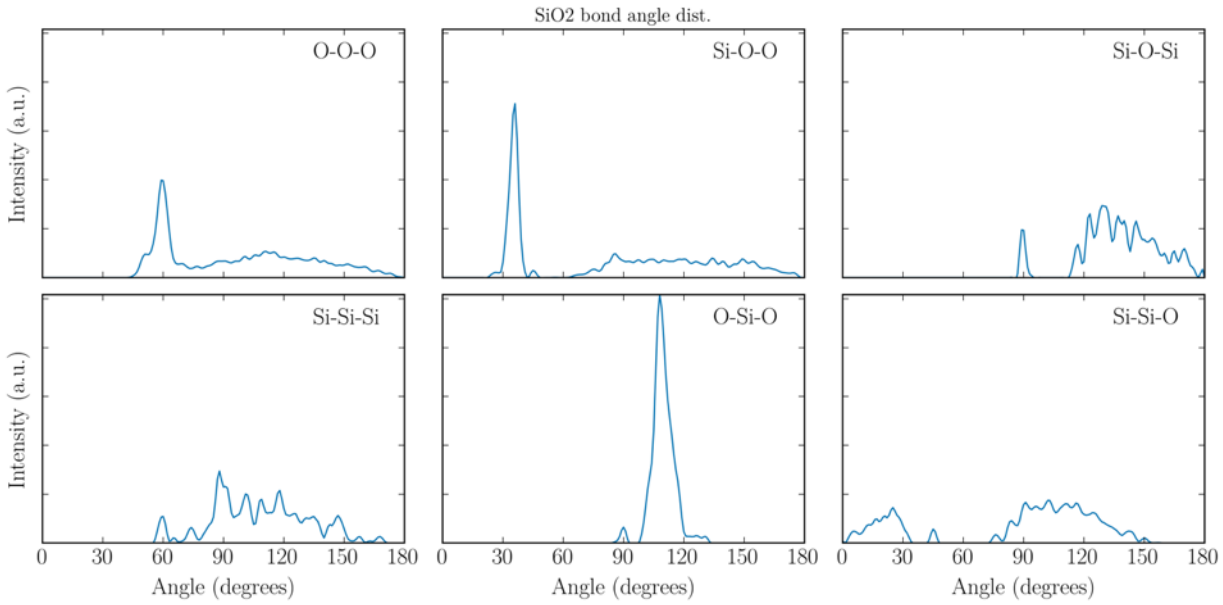

fig. S69. Bond-angle distribution functions of amorphous configurations. Bond angle distribution functions of AIMD-generated amorphous SiO_2.

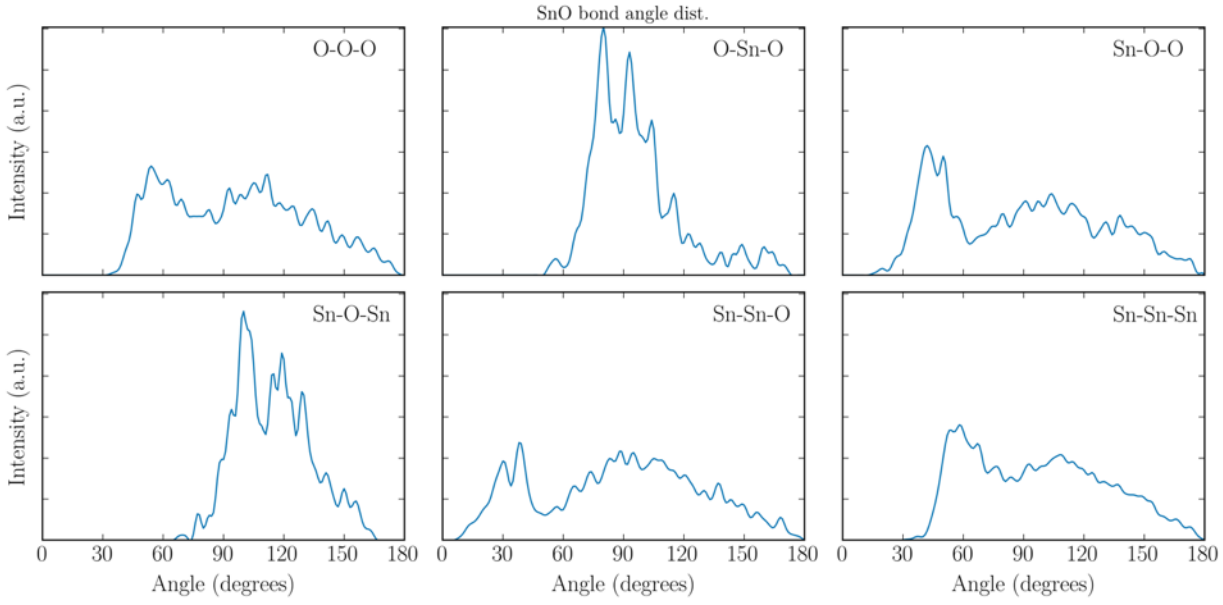

fig. S70. Bond-angle distribution functions of amorphous configurations. Bond angle distribution functions of AIMD-generated amorphous SnO.

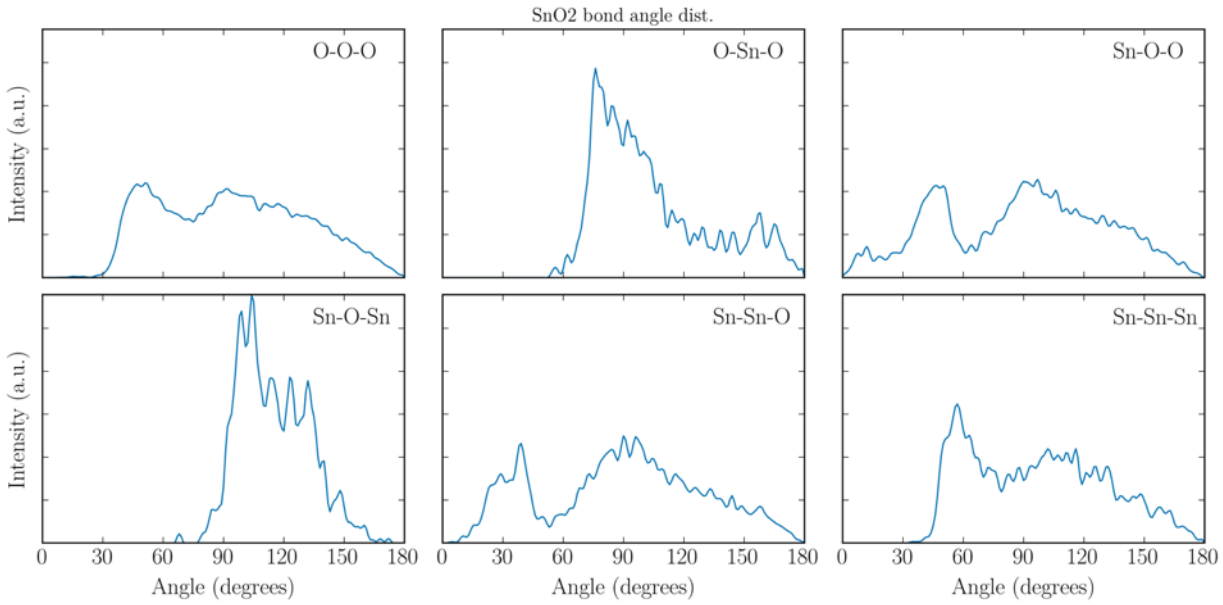

fig. S71. Bond-angle distribution functions of amorphous configurations. Bond angle distribution functions of AIMD-generated amorphous SnO_2.

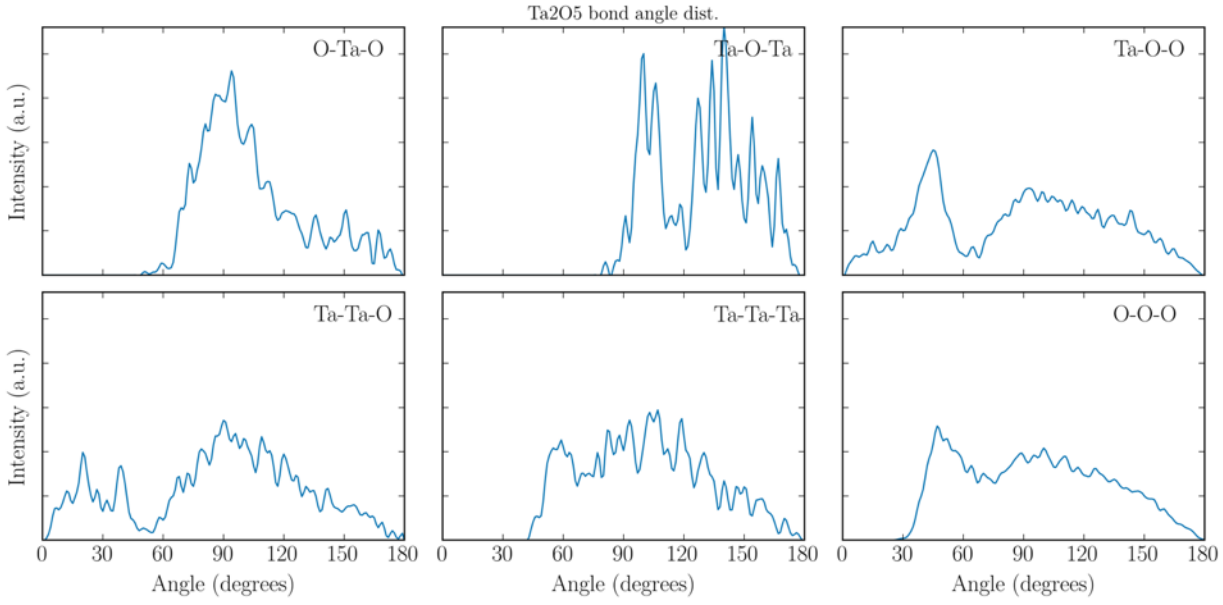

fig. S72. Bond-angle distribution functions of amorphous configurations. Bond angle distribution functions of AIMD-generated amorphous Ta_2O_5.

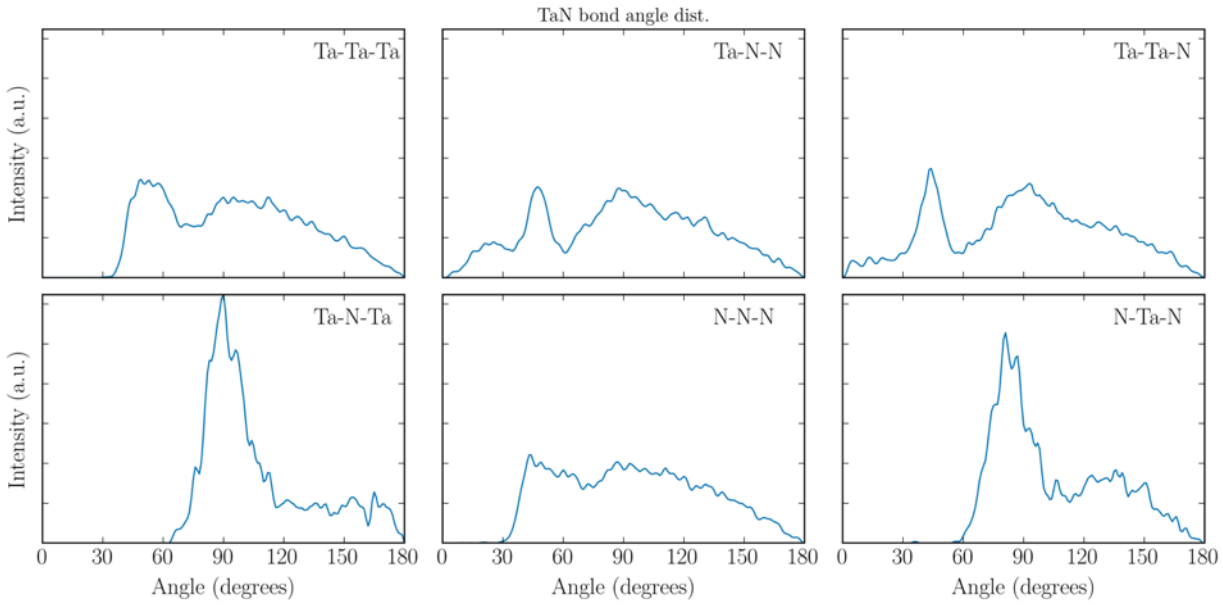

fig. S73. Bond-angle distribution functions of amorphous configurations. Bond angle distribution functions of AIMD-generated amorphous TaN.

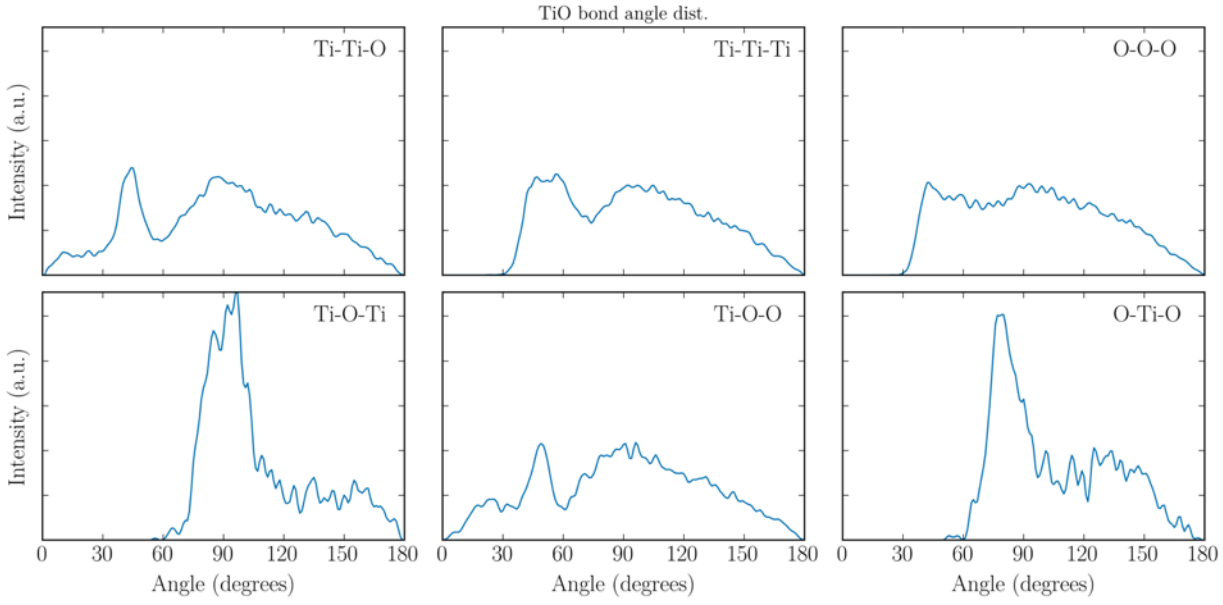

fig. S74. Bond-angle distribution functions of amorphous configurations. Bond angle distribution functions of AIMD-generated amorphous TiO.

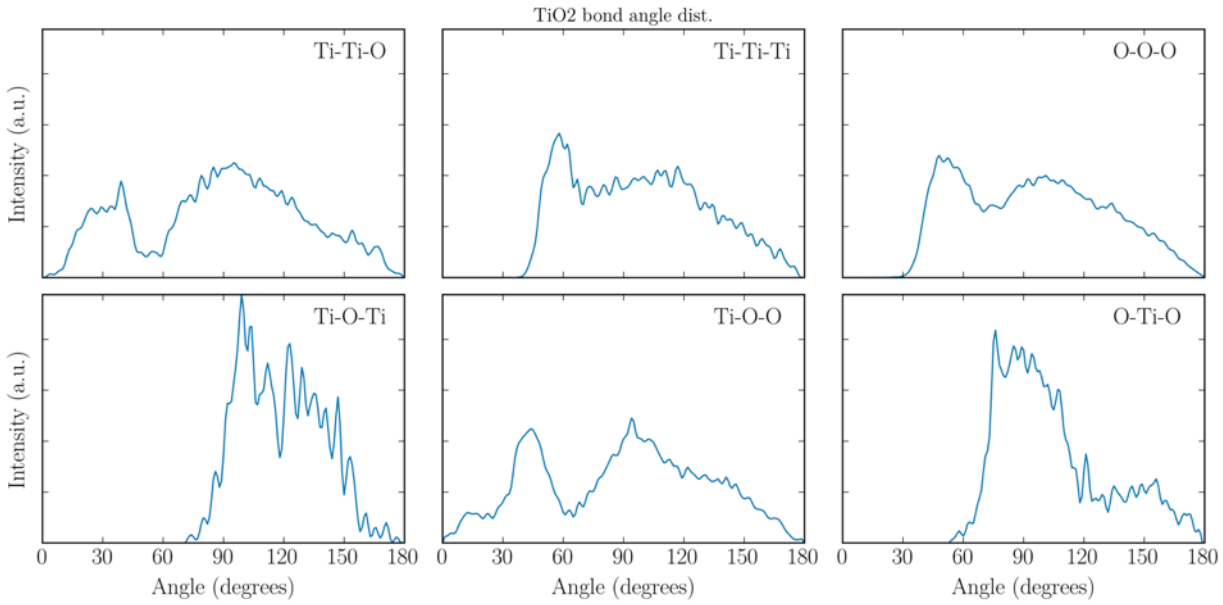

fig. S75. Bond-angle distribution functions of amorphous configurations. Bond angle distribution functions of AIMD-generated amorphous TiO_2.

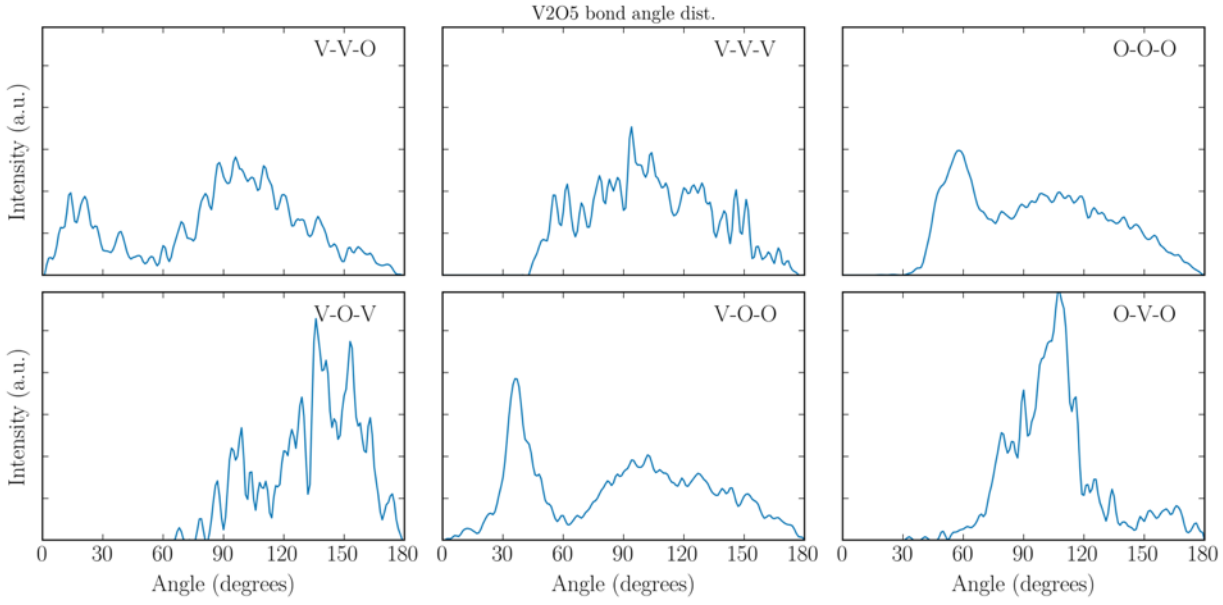

fig. S76. Bond-angle distribution functions of amorphous configurations. Bond angle distribution functions of AIMD-generated amorphous V_2O_5.

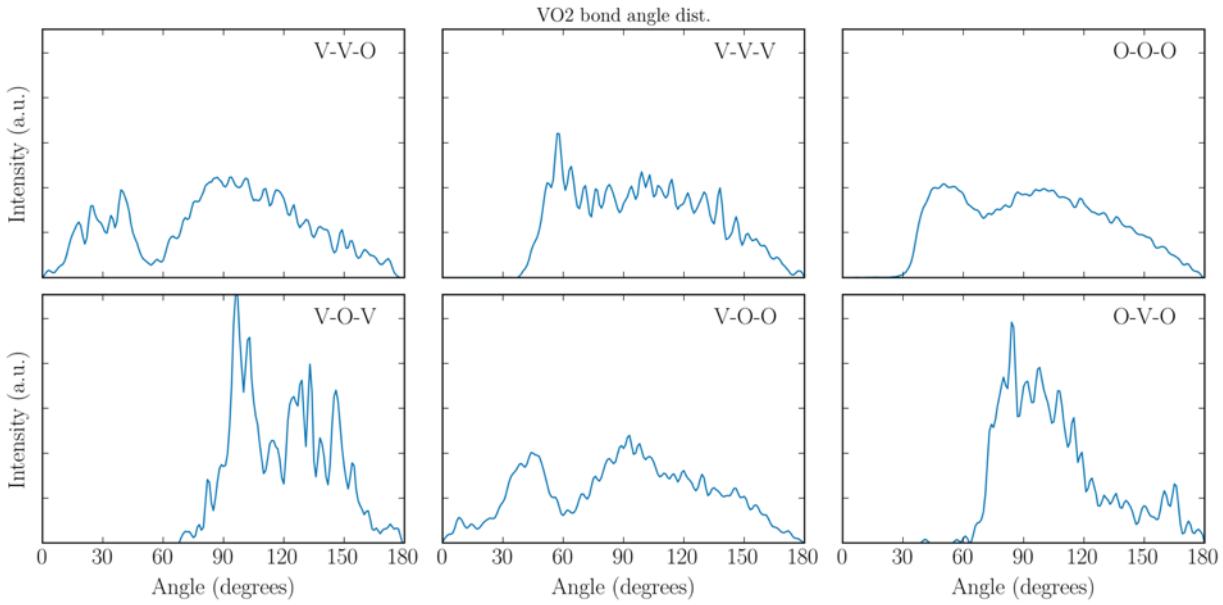

fig. S77. Bond-angle distribution functions of amorphous configurations. Bond angle distribution functions of AIMD-generated amorphous VO_2.

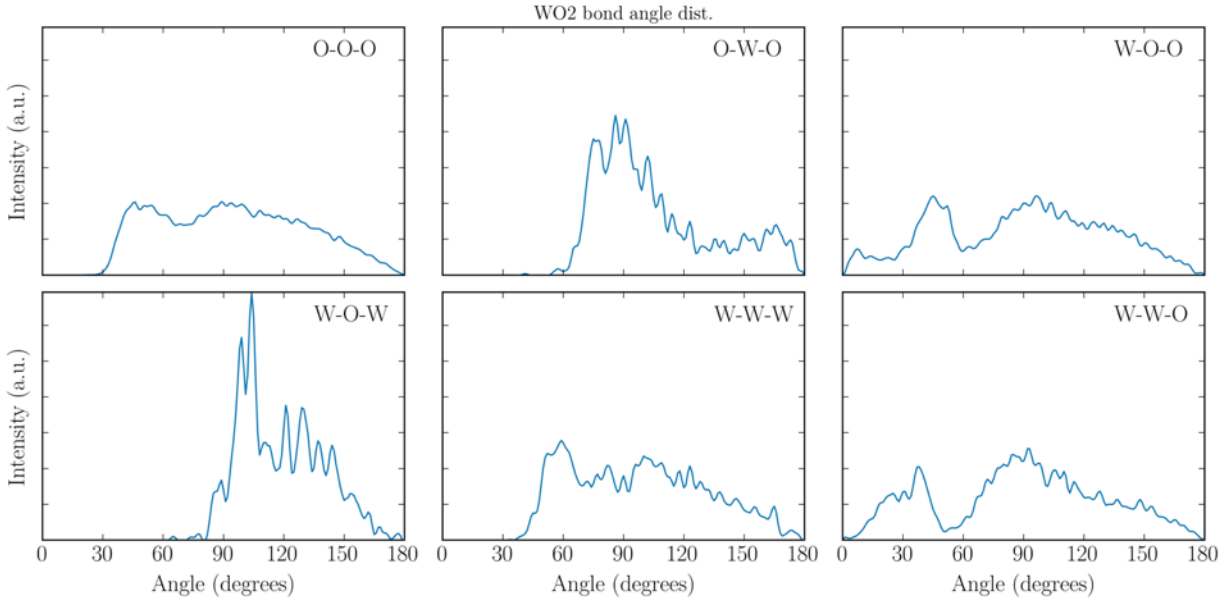

fig. S78. Bond-angle distribution functions of amorphous configurations. Bond angle distribution functions of AIMD-generated amorphous WO_2.

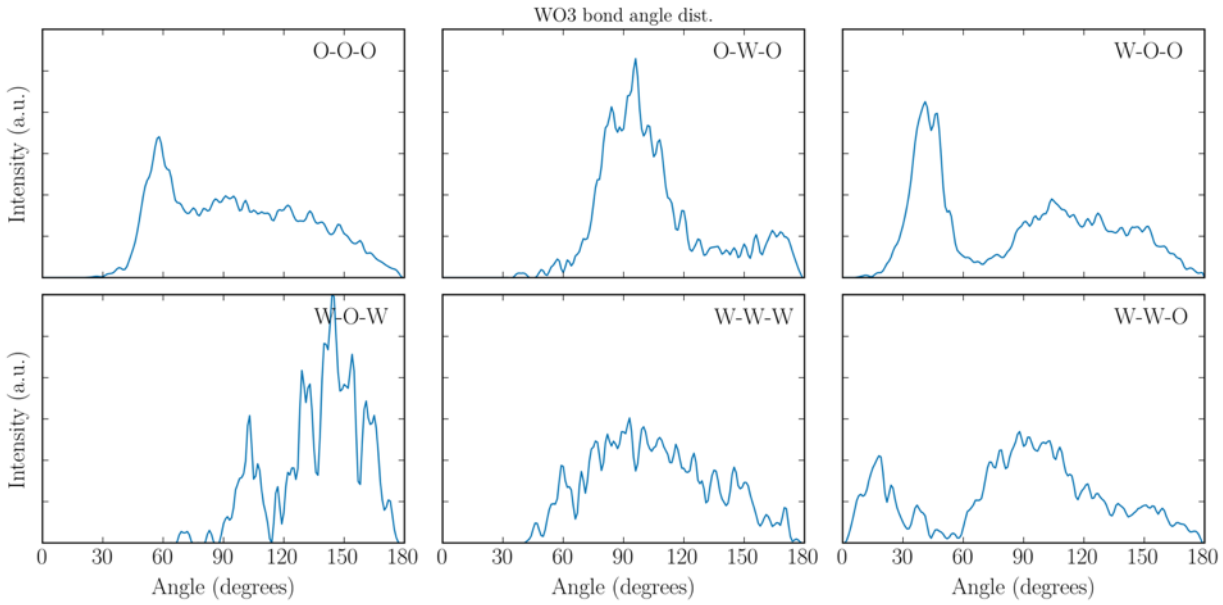

fig. S79. Bond-angle distribution functions of amorphous configurations. Bond angle distribution functions of AIMD-generated amorphous WO_3.

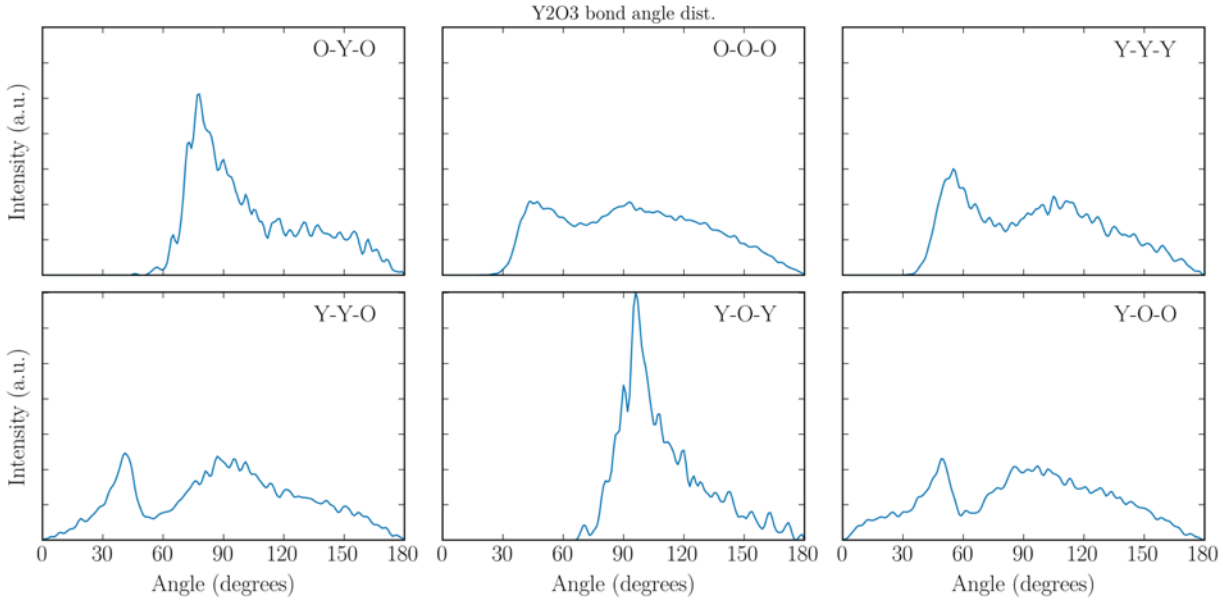

fig. S80. Bond-angle distribution functions of amorphous configurations. Bond angle distribution functions of AIMD-generated amorphous Y_2O_3.

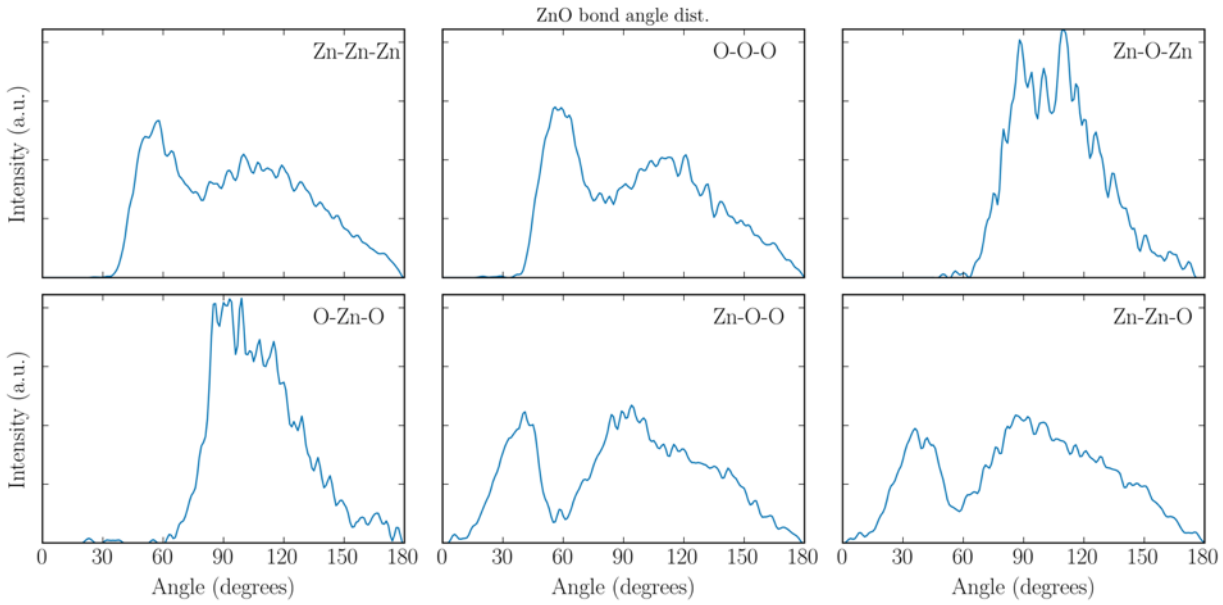

fig. S81. Bond-angle distribution functions of amorphous configurations. Bond angle distribution functions of AIMD-generated amorphous ZnO.

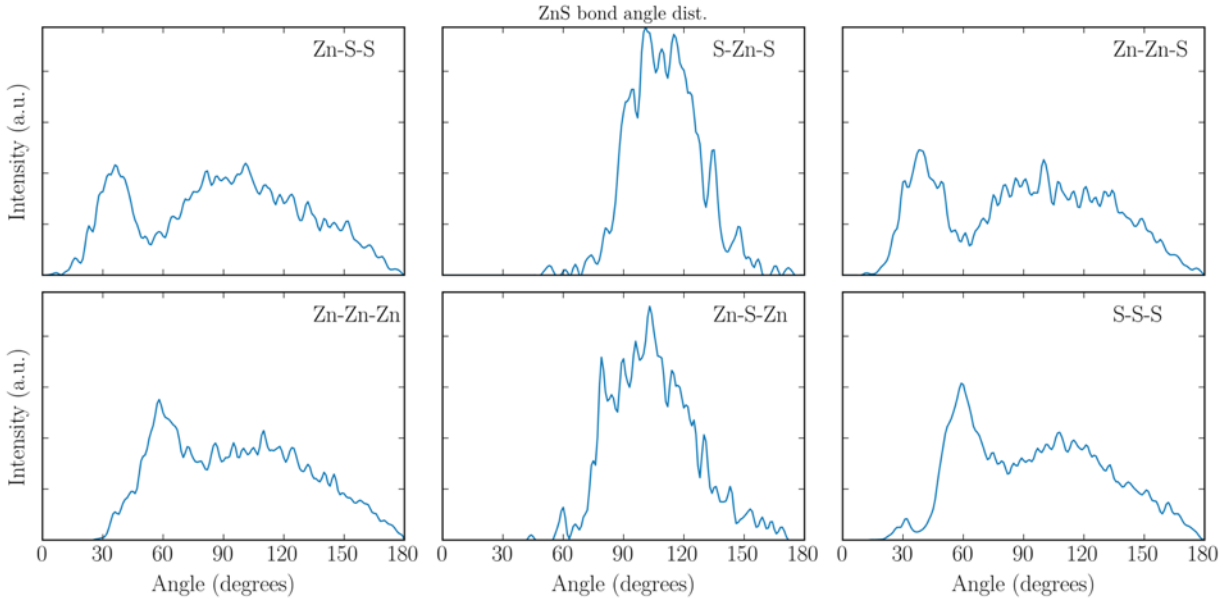

fig. S82. Bond-angle distribution functions of amorphous configurations. Bond angle distribution functions of AIMD-generated amorphous ZnS.

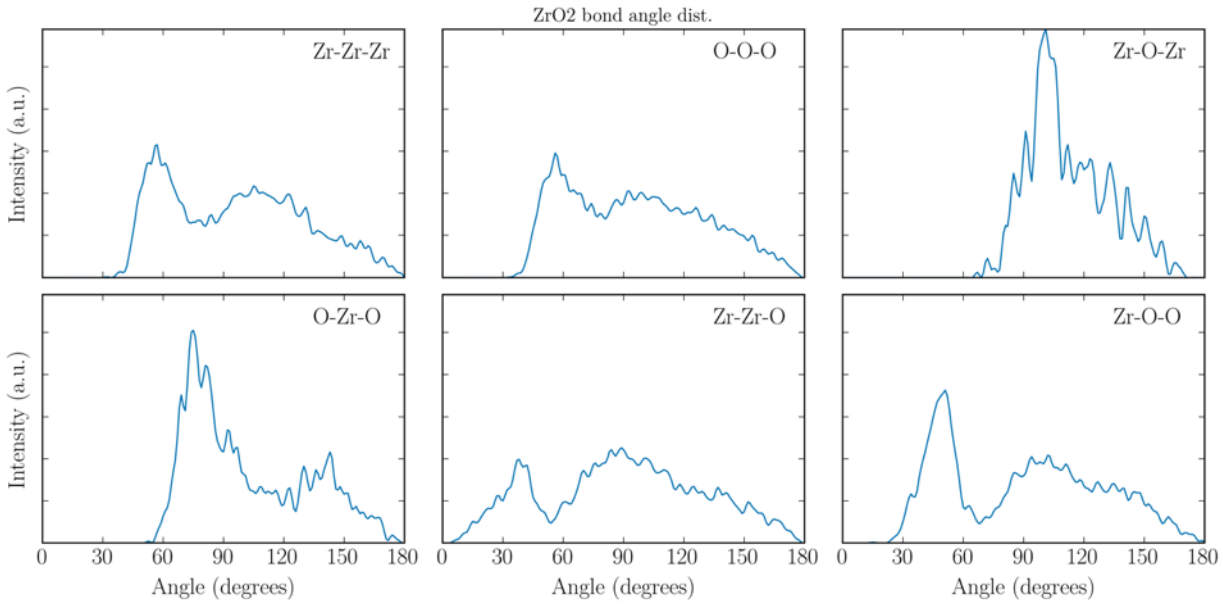

fig. S83. Bond-angle distribution functions of amorphous configurations. Bond angle distribution functions of AIMD-generated amorphous ZrO_2.

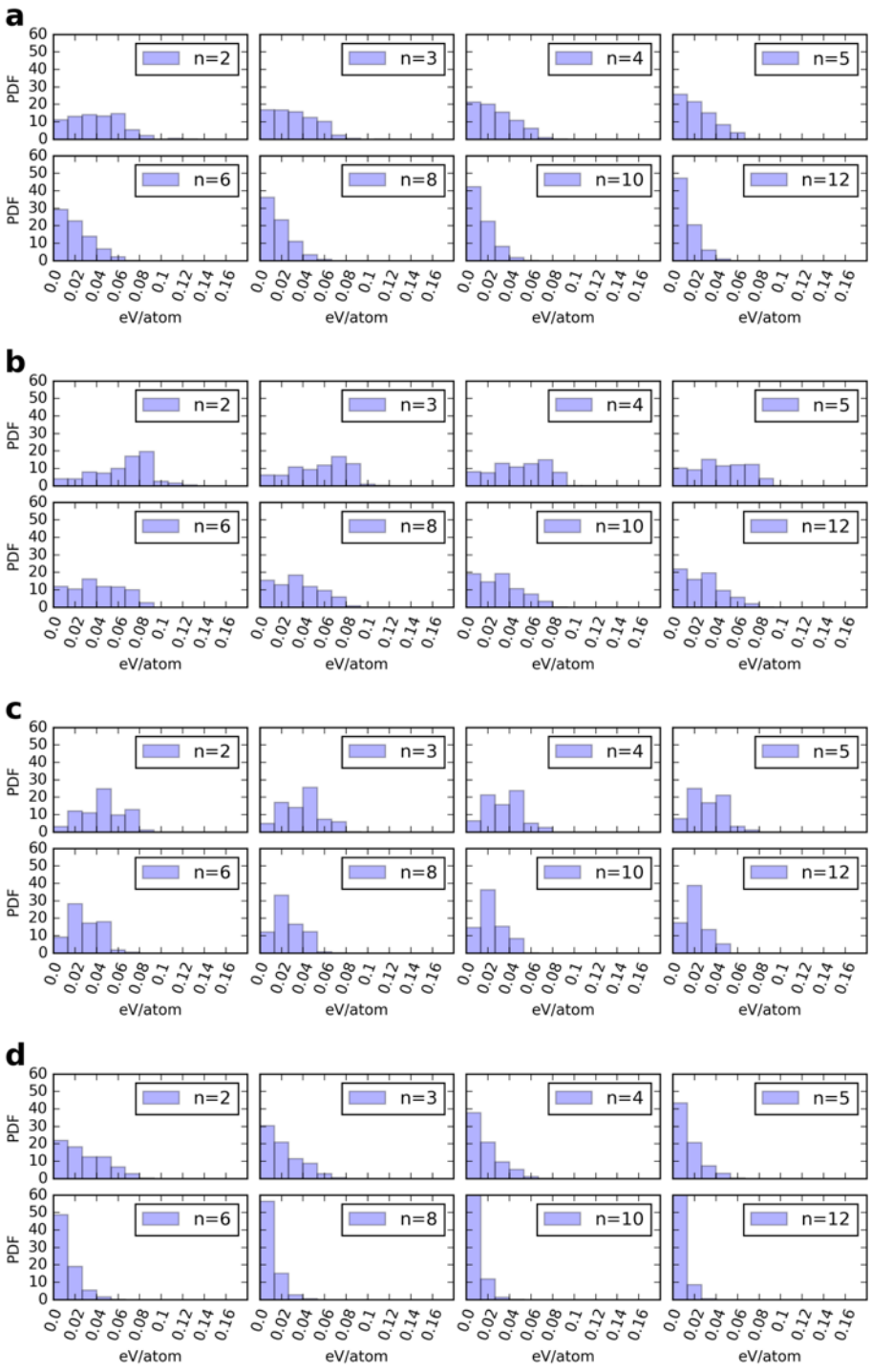

fig. S84. Amorphous limit sampling probability. Amorphous limit sampling probability. Probability density functions (PDFs) for sampling the minimum energy amorphous configuration taken by randomly sampling n configurations 10,000 times from larger populations of size N for (**a**) Al_2O_3 with N = 50, (**b**) GaN with N = 35, (**c**) V_2O_5 with N = 46 and (**d**) ZnS with N = 44.

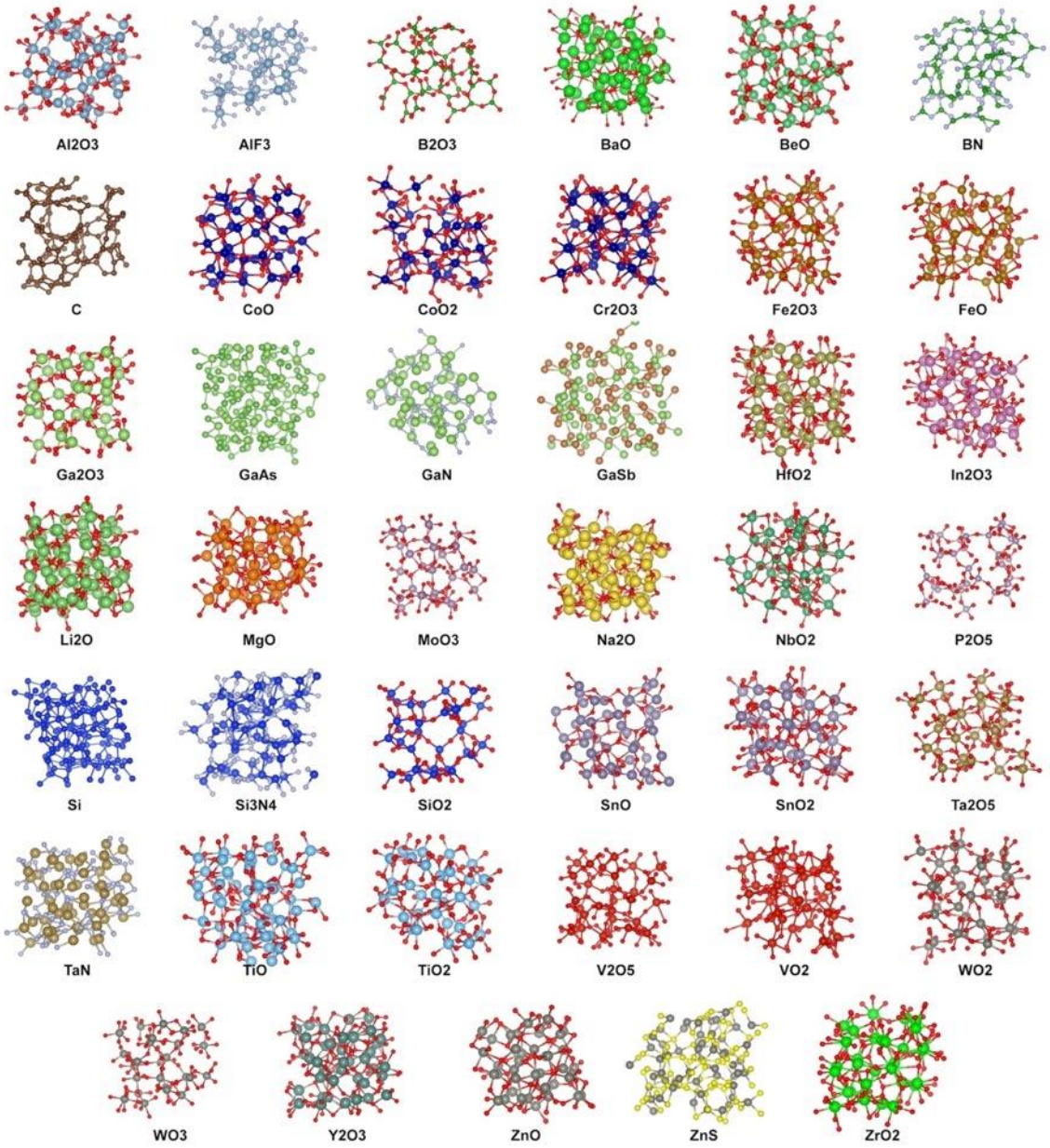

fig. S85. Snapshots of atomic structures of amorphous materials. Snapshots of atomic structures of amorphous materials. One representative configuration is shown for each material system for illustration purposes.

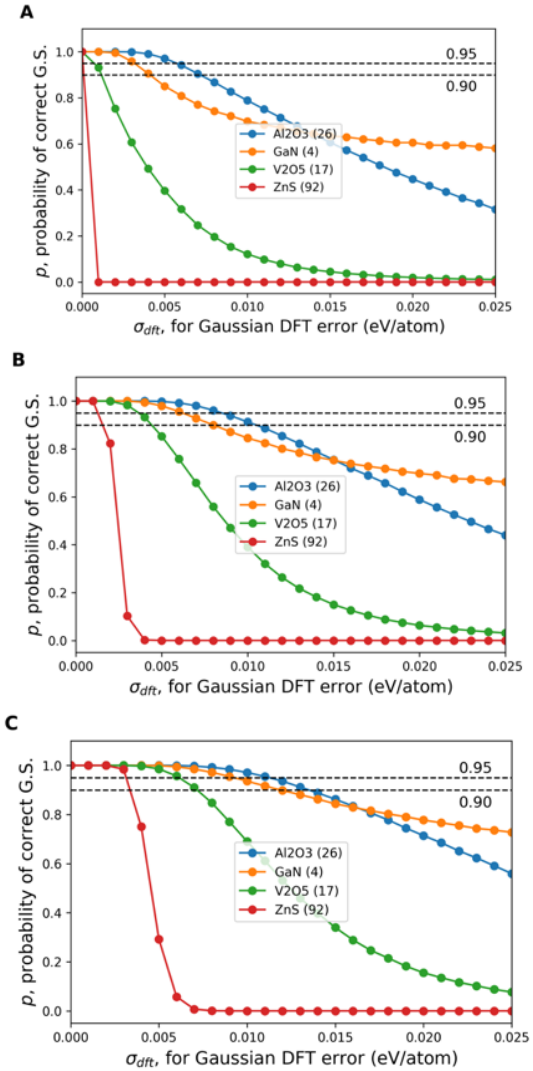

fig. S86. Probability of finding the correct, observed ground states. Probability of finding the correct, observed groundstate in Al_2O_3, GaN, V_2O_5 and ZnS polymorphic systems (**A**) exactly as the DFT groundstate, or within (**B**) 5 meV/atom and (**C**) 10 meV/atom of the DFT groundstate, as a function of standard deviation (σ) of hypothetical, Gaussian-distributed random errors in relative DFT energies. The number of entries in each system is given in parentheses. For each σ data-point of a chemical system, we perturbed all the entries available for that system in the Materials Project database with random errors drawn from a Gaussian distribution corresponding to that σ, repeated for 10^5 trials [in analogy with the analysis of effect of formation energy errors on convex hull (*16*)]. From these simulations, we evaluated the probability that the correct ground state is found (exactly or within the given tolerances) for a given σ. The tolerance accounts for not having an infinite precision in DFT simulations, and possible systematic errors. A larger tolerance gives slower decaying probabilities, and larger uncertainties for DFT energies.

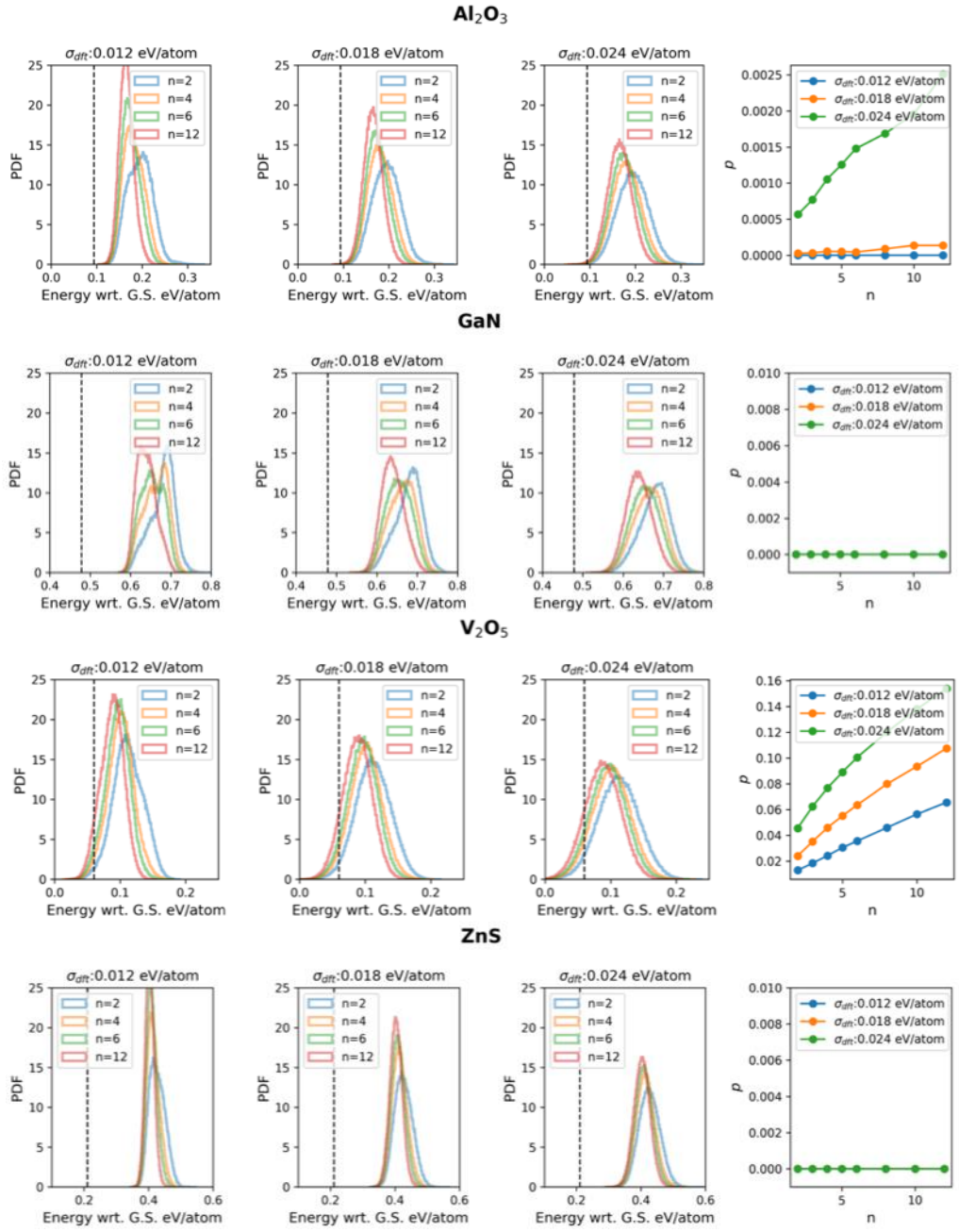

fig. S87. PDFs from aggregated uncertainties in the amorphous limit classification of crystalline polymorphs. Probability density functions (PDFs) from aggregated uncertainties in the amorphous limit classification of crystalline polymorphs. First three panels show PDFs obtained from statistical simulations with random sampling of amorphous energies with sample size *n* with DFT errors added by sampling from Gaussian distributions with a standard-deviation of 0.012, 0.018 and 0.024 eV/atom. The dashed-lines show the highest-energy polymorph reported among all experimentally synthesized phases (as obtained from the ICSD) in each system. The right-most panel shows the corresponding probabilities that at least one synthesizable compound is misclassified as not synthesizable.

table S1. The amorphous limits for the synthesizability of polymorphs. The amorphous limits (distance to groundstate energies) for the synthesizability of material polymorphs. These limits are calculated by the sampling amorphous structures quenched from ab-initio molecular dynamics generated liquids. By construction, the limits are fail-safe; that is, they cannot classify a synthesizable polymorph as otherwise, and by sampling more amorphous configurations, the limit can only become lower. Limits listed here are relevant on the *G*–*T* domain close zero pressure.

Material	Amorphous limit (eV/atom)		Material	Amorphous limit (eV/atom)
Al_2O_3	0.154		Na_2O	0.147
AlF_3	0.173		NbO_2	0.209
B_2O_3	0.063		P_2O_5	0.177
BaO	0.172		Si	0.310
BeO	0.258		Si_3N_4	0.359
BN	0.621		SiO_2	0.114
C	0.933		SnO	0.190
CoO	0.285		SnO_2	0.275
CoO_2	0.200		Ta_2O_5	0.165
Cr_2O_3	0.349		TaN	0.463
Fe_2O_3	0.246		TiO	0.259
FeO	0.246		TiO_2	0.161
Ga_2O_3	0.148		V_2O_5	0.067
GaAs	0.409		VO_2	0.208
GaN	0.616		WO_2	0.488
GaSb	0.291		WO_3	0.223
HfO_2	0.210		Y_2O_3	0.225
In_2O_3	0.268		ZnO	0.246
Li_2O	0.152		ZnS	0.399
MgO	0.254		ZrO_2	0.202
MoO_3	0.136			

Caption for Database S1 (separate file)

database S1. Energies of amorphous configurations. Total energies (eV/atom) of amorphous configurations as obtained with the AIMD+DFT procedure described in Materials and Methods, available as a *json* dictionary.